

Vertical transport and domain formation in multiple quantum wells

Andreas Wacker

*Mikroelektronik Centret, Danmarks Tekniske Universitet, DK-2800 Lyngby,
Denmark*

email: wacker@mic.dtu.dk

to appear in:

Theory of Transport Properties of Semiconductor Nanostructures

edited by Eckehard Schöll
(Chapman and Hall, in preparation)

In this book article effects related to the vertical transport in weakly coupled multiple quantum wells are reviewed. A self-contained microscopical model for the calculation of the well-to-well currents without any fittings parameters is presented. The model exhibits the well-known peaks in the current-field relation in quantitative agreement with experiments. This local current-field relation is used as an input for the calculation of the transport in the extended structure consisting of many periods. Here both the formation of stationary field domains as well as self-sustained current oscillations are found in good agreement with experimental data. The underlying physics of these nonlinear phenomena is discussed in detail.

0 Introduction

Today's growth techniques allow the construction of semiconductor structures where layers of different semiconductors (exhibiting similar lattice constants) can be grown on each other with the interface being well defined within one atomic monolayer. If two such layers alternate periodically one obtains a periodic structure with an artificial period d in the growth direction (which is defined to be the z -direction). This leads to spatial variations in the conduction and valence band of the material as sketched in Fig. 1. Considering only conduction band states in the following, the region with lower conduction band is called 'well' and the region with higher conduction band 'barrier'. An extended discussion of various aspects of such structures can be found in Ref. [1]. In this chapter the vertical electronic transport (i.e., in z -direction) is considered for such structures.

If we consider the electronic properties of such a structure, there are two different approaches. In the first approach one may consider the full structure as an artificial lattice. The energy spectrum can be calculated analogously to the Kronig-Penney model (which is discussed in almost all solid-state physics textbooks) resulting in the appearance of energy bands and energy gaps as sketched in Fig. 1. Due to this analogy with the atomic lattice of lattice constant a_L such semiconductor structures are often called superlattices. The corresponding eigenfunctions are the usual Bloch functions which extend over the whole superlattice. The Bloch functions are labeled with the Bloch vector q which is restricted to the Brillouin zone $-\pi/d < q < \pi/d$. This range is much smaller than the Brillouin zone $-\pi/a_L < q < \pi/a_L$ of the atomic lattice as $d \gg a_L$. Therefore these new bands are called minibands. If an electric field is applied, the Bloch functions are accelerated and the transport can be treated analogously to the usual transport in bulk systems [2]. Due to the short Brillouin zone many special effects like Bloch oscillations can be found here which are not accessible in bulk systems as discussed in the preceding chapter.

In the second approach one may consider the wells to be isolated from each other as a first approximation and calculate the eigenstates within each well. This yields a sequence of energy levels and localized wave functions for each well. Such a structure is usually called a multiple quantum well. Of course

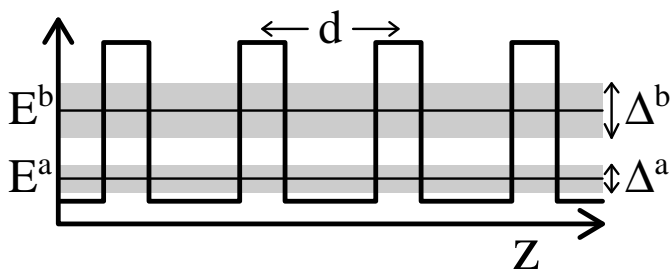


Figure 1: Sketch of the conduction band $E_c(z)$ with minibands $\nu = a, b$

this approach only makes sense if the coupling between different wells is weak and can be calculated perturbatively. Thinking in terms of Fermi's golden rule, there will be transitions between the levels in different wells yielding sequential tunnelling. Due to energy conservation this tunnelling takes only place if the energy levels align and strong resonances [3] are likely to occur if the relative height of the levels in different wells is varied by a voltage applied in the z -direction.

The width of these resonances is related to scattering processes of the electrons inside the wells. In Ref. [4] this feature was used to determine the electron-electron scattering rate from the transport between two weakly coupled quantum wells. This shows that a modelling of scattering processes is necessary for a calculation of the current in such structures and opens the possibility for checking theoretical concepts as well as investigating the significance of various scattering mechanisms by comparison with experimental data.

These resonances yield strong nonlinearities in the local current-field relation. If we now have a long periodic sequence of these coupled quantum wells the full system is a good example of an extended nonlinear system. This leads to the appearance of complicated current-voltage characteristics exhibiting an almost periodic sequence of branches due to the formation of electric field domains as well as to self-sustained oscillations due to moving domains. As the periodicity of the structure is an important feature for the translational invariance, these structures are frequently called superlattices for weak coupling as well. If the translational invariance is broken due to an insufficient control of the growth conditions the branches lose their periodic structure, and information about the actual structure can be obtained from measurements of the current-voltage characteristics.

The first section of this chapter is devoted to the classification of the different regimes depending on the coupling between the wells. In the second section a transport model for weakly coupled quantum wells is presented which allows a microscopic calculation of the current without any fitting parameters. In the third chapter this model is extended in order to describe domain formation. The fourth section is on the influence of deviations from the periodic structure of the superlattice and the fifth section refers to self-sustained oscillations. Finally, details of the calculations will be given in the sixth section.

1 The different transport regimes

In this section the precise meaning of weakly and strongly coupled quantum wells is discussed.

Assuming ideal interfaces the semiconductor structure is translational invariant within the x and y direction perpendicular to the growth direction. Therefore the x, y dependence can be separated by the ansatz $e^{i\mathbf{k}\cdot\mathbf{r}}$ where \mathbf{k} and \mathbf{r} are vectors within the two-dimensional (x, y) plane. (The effects due to the atomic periodicity of the lattice are treated within the envelope function formalism [5] assuming a parabolic subband.) Within the z -direction we have

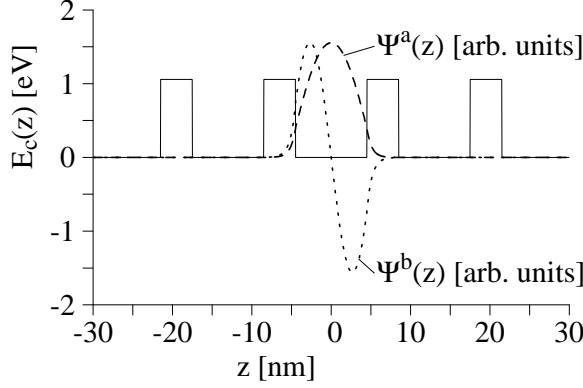


Figure 2: Conduction band $E_c(z)$ together with the Wannier functions calculated for the two lowest subbands.

an artificial period d leading to energy states E_q^ν characterized by the miniband index ν and the quasi-wave vectors $-\pi/d < q \leq \pi/d$. The energies as well as the wave-functions $\varphi_q^\nu(z)$ can be calculated numerically analogously to the well-known Kronig-Penney model. For a given miniband ν the energy E_q^ν has a mean value $E^\nu = d/(2\pi) \int_{-\pi/d}^{\pi/d} dq E_q^\nu$ and varies within the miniband width $\Delta^\nu = \text{Max}_q(E_q^\nu) - \text{Min}_q(E_q^\nu)$ as sketched in Fig. 1.

From the Bloch functions $\varphi_q^\nu(z)$ the Wannier functions $\Psi^\nu(z - nd)$ defined by

$$\Psi^\nu(z - nd) = \sqrt{\frac{d}{2\pi}} \int_{-\pi/d}^{\pi/d} dq e^{-inqd} \varphi_q^\nu(z) \quad (1)$$

can be constructed. They are real and localized in well n for an appropriate choice of the complex phase for $\varphi_q^\nu(z)$ [6]. An example is shown in Fig. 2. Using the Fourier expansion

$$E_q^\nu = E^\nu + \sum_{h=1}^{\infty} 2T_h^\nu \cos(hdq) \quad (2)$$

one obtains the following Hamiltonian in second quantization

$$\hat{H} = \sum_{n,\nu} E^\nu c_n^{\nu\dagger} c_n^\nu + \sum_{h=1}^{\infty} \left(T_h^\nu c_{n+h}^{\nu\dagger} c_n^\nu + T_h^\nu c_{n-h}^{\nu\dagger} c_n^\nu \right) \quad (3)$$

for the creation $c_n^{\nu\dagger}$ and annihilation c_n^ν operators of the Wannier functions $\Psi^\nu(z - nd)$. As the Wannier functions are linear combinations of Bloch functions with different energies, they are no stationary states. Neglecting terms with $h > 1$ the time evolution of the annihilation operators is given by

$$i\hbar \frac{d}{dt} c_n^\nu = T_1^\nu (c_{n+1}^\nu + c_{n-1}^\nu) . \quad (4)$$

For the initial condition $c_n^\nu(t=0) = \delta_{n,0}c_0^\nu$ this has the solution

$$c_n^\nu(t) = i^{-n} J_n \left(\frac{2T_1^\nu}{\hbar} t \right) c_0^\nu \quad (5)$$

where $J_n(x)$ is the Bessel function of order n . Since $\sum_{n=-\infty}^{\infty} n^2 (J_n(x))^2 = x^2/2$ the average extension $n_a(t)$ as a function of time is found to be

$$n_a(t) = \sqrt{\langle n^2 \rangle} = \frac{\sqrt{2}T_1}{\hbar} t. \quad (6)$$

This is obviously a coherent process. In a real semiconductor structure there will be scattering (characterized by a scattering time τ_{sc}) destroying the coherent evolution¹ given by Eq. (4). If $n_a(\tau_{sc}) \ll 1$ holds, the phase coherence is completely lost during the spread and the states of adjacent wells will not maintain a fixed phase relation. In this case the transitions can be described by sequential tunnelling between the Wannier states with loss of phase between different tunnelling events. Defining $\Gamma = \hbar/\tau_{sc}$ one therefore may use the picture of

sequential tunnelling for $T_1 \ll \Gamma/\sqrt{2}$.

(7)

If, on the other hand, the extended Bloch functions shall be a reasonable basis set, the phase coherence has to be maintained over a larger number of quantum wells. This gives $n_a(\tau_{sc}) \gg 1$ as a first necessary condition. But a further complication arises if an electric field F is applied in the z direction. As discussed in the preceding chapter of this book the eigenvalues of the Hamiltonian take discrete values $E^\nu - neFd$ which is called the Wannier-Stark (WS) ladder. The corresponding eigenfunctions $\phi_{WS}^\nu(z - nd)$ are localized around well n . Within the one band limit they are given by

$$\phi_{WS}^\nu(z) = \sum_n J_n \left(\frac{2T_1^\nu}{eFd} \right) \Psi^\nu(z - nd). \quad (8)$$

(See, e.g., Ref. [7], where also the coupling between different bands is discussed.) Then the spatial extension of the WS-states is given by

$$n_{WS} = \sqrt{\langle n^2 \rangle} = \frac{\sqrt{2}T_1}{eFd}. \quad (9)$$

If now n_{WS} becomes small, the electrons are localized and the use of extended Bloch functions does not make any sense. This provides the second condition $n_{WS} \gg 1$ for the Bloch functions to be an appropriate basis set of wave functions. Thus it only makes sense to speak about

minibands for $T_1 \gg \Gamma/\sqrt{2}$ and $T_1 \gg eFd\sqrt{2}$.

(10)

¹This scattering can be a phase breaking process such as scattering with phonons. But also elastic scattering processes at impurities or interface roughness will contribute here because they destroy the translational invariance of the superlattice, which is both the justification for the existence of the Bloch functions and a WS state.

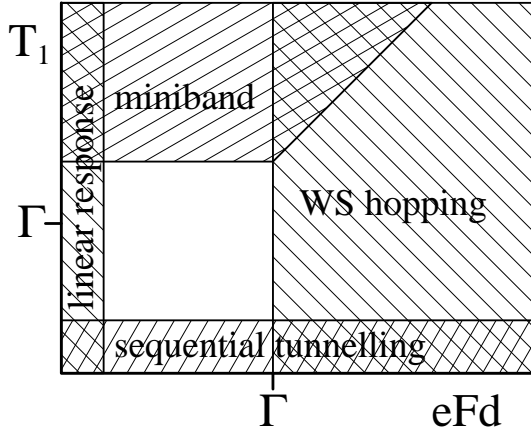


Figure 3: Sketch of the regimes where different approaches are valid

As a third basis set the Wannier-Stark functions $\phi_{\text{WS}}^l(z - nd)$ may be used if an electric field is applied. They make sense if coherence is maintained within their extension, i.e., if $n_{\text{WS}} < n_a(\tau_{\text{sc}})$. Therefore the transport can be described by

$$\boxed{\text{WS hopping for } eFd > \Gamma.} \quad (11)$$

These different regimes of validity are sketched in Fig. 3 where the condition $a \ll b$ has been translated to $a < b/2$ for illustrative purpose.

How can the electric transport be described if an electric field F is applied in the z direction? For $F = 0$ the system should be in equilibrium and no current I flows. For small fields the current should increase with F . (This may be calculated by linear response which is given by the Kubo formula for a quantum system. See, e.g., chapter 5, where the application of the Kubo formula has been described for the Coulomb drag.) Now it is an important feature of both superlattices and multiple quantum wells that for larger fields there is a range with negative differential conductivity $dI/dF < 0$ (NDC). This can be easily understood within the Wannier-Stark picture. As the WS-states are orthogonal, transitions between them have to be caused by scattering events. Now the matrix element for a given scattering element depends on the spatial overlap of the eigenfunctions. With increasing field the Wannier-Stark states become more and more localized as can be seen from Eq. (9). Therefore the matrix element for the scattering is decreased and the hopping rate is diminished [8, 9]. As the WS approach is not justified for low electric fields (see Fig. 3) an Ohmic behaviour for low fields could not be observed within this model [9].

In the validity range of (10) the basis of Bloch functions may be used. Due to an electric field the Bloch waves are accelerated according to $\hbar\dot{q} = eF$. Like in the standard transport theory for bulk systems a positive conductivity is found for low electric fields. But for higher fields the Bloch vector q may run through the whole Brillouin zone $2\pi/d$ if $eF\tau_{\text{sc}}/\hbar > 2\pi/d$ holds. Then the electrons perform a periodic motion in both q and z space which is called the Bloch

oscillation. A quantitative analysis within various approaches [2, 10, 11, 12] reveals

$$I \sim \frac{eFd}{(eFd)^2 + \Gamma^2}. \quad (12)$$

This yields positive differential conductivity for $eFd < \Gamma$ and negative differential conductivity for larger fields which is confirmed by experimental data (see, e.g., [13, 14]). For large F there is $I \sim 1/F$. This behaviour is also found from the WS-hopping model for $eFd < \Delta = 4T_1$ [9] which can be easily understood from Fig. 3 as this condition includes the region where both approaches are valid. This is an explicit example of the more general equivalence between the Wannier-Stark picture and the Bloch oscillation picture discussed in chapter 9 of this book.

In case of weakly coupled multiple quantum wells $T_1 \ll \Gamma/\sqrt{2}$ NDC has been observed experimentally as well [15]. Here we can consider the electronic states to be the levels of the single quantum wells which will exhibit a certain width Γ due to scattering. The tunnelling between the wells is caused by the coupling T_1 . Due to energy conservation a significant current between adjacent wells may flow if the levels are aligned within accuracy Γ . Therefore NDC is likely to appear if the disalignment eFd becomes larger than Γ [16, 17]. This will be modelled quantitatively in the next section.

For the white region of Fig. 3 between these two limits the situation is more complicated. Here Laikhtman and Miller [18] were able to show that Eq. (12) holds provided the electron temperature is much larger than T_1 and eFd .

In an extended system the existence of an NDC region typically causes oscillatory behaviour due to travelling field domains (see, e.g., [19]). For the miniband regime this has been studied theoretically quite early in Refs. [20, 21, 22] and recently also experimentally [23, 24]. Note that these travelling domain oscillations are self-sustained in Ref. [24] while for the usual Bloch oscillations only transient oscillations are found (see, e.g., Ref. [25]). The same type of oscillations has been recently found in the regime of sequential tunnelling both experimentally [26, 27, 28] and by numerical simulations [29, 30]. An analytic treatment of the oscillation mode is given in Refs. [31, 32]. Under certain conditions chaotic oscillations occur as well [33, 34].

For weakly coupled multiple quantum wells an additional scenario occurs, which has been extensively studied in the last decade: As the electronic states are localized within single wells the domain boundary (which are charge accumulation layers) can be trapped in a single quantum well and a stationary stable domain is formed. As the domain boundary may be located in any well a periodic sequence of branches appears in the current-voltage characteristic. This effect has been observed experimentally by many groups [35]- [49]. Theoretically such effects can be studied by combining rate equations between the wells and Poisson's equation. Such an approach has already been performed in Refs. [50, 51]. Nevertheless, to my knowledge, the full current-voltage characteristic exhibiting the domain structure could first be resolved qualitatively in Ref. [52] for slim superlattices exhibiting a few electrons per well and in Refs. [53, 54] for two-dimensional wells. A full quantitative calculation has been

presented recently [55, 56] for different multiple quantum wells yielding quantitative agreement with experimental data without using any fitting parameters. This model will be presented in the next sections.

2 Modelling of the transport between weakly coupled quantum wells

In this section I want to show how the currents between the wells can be calculated from a microscopic model. Furthermore I present some simplifications in order to obtain estimates for the current. The numerical calculations are performed with the data of the sample used in Refs. [26, 40] exhibiting $N = 40$ GaAs wells of width $w = 9$ nm between 41 AlAs barriers of width $b = 4$ nm. The wells are n-doped with a doping density of $N_D = 1.5 \times 10^{11}/\text{cm}^2$ per well. Details of the specific calculations outlined in this section are given in section 6.

As discussed in the first section, for weakly coupled quantum wells the products of Wannier functions $\Psi^\nu(z - nd)$, localized in well n , and plane waves $e^{i\mathbf{k}\cdot\mathbf{r}}$ form a reasonable basis set of wave functions. Now we restrict ourselves to the lowest two levels denoted by $\nu = a, b$. The respective annihilation operators are denoted by $a_n = c_n^a$ and $b_n = c_n^b$. Furthermore we add the contribution $-eFz$ due to a homogeneous electric field F in the Hamiltonian (3) where $e < 0$ is the charge of the electron. Restricting ourselves to coupling between neighbouring wells ($h = 1$) we obtain the Hamiltonian $\hat{H} = \hat{H}_0 + \hat{H}_1 + \hat{H}_2$:

$$\begin{aligned} \hat{H}_0^{\text{res}} = \sum_{n,\underline{k}} & [(E^a + E_k - eFdn)a_n^\dagger(\underline{k})a_n(\underline{k}) \\ & + (E^b + E_k - eFdn)b_n^\dagger(\underline{k})b_n(\underline{k})] \end{aligned} \quad (13)$$

$$\begin{aligned} \hat{H}_1^{\text{res}} = \sum_{n,\underline{k}} & [T_1^a a_{n+1}^\dagger(\underline{k})a_n(\underline{k}) + T_1^b b_{n+1}^\dagger(\underline{k})b_n(\underline{k}) \\ & - eFR_1^{ab}a_{n+1}^\dagger(\underline{k})b_n(\underline{k}) - eFR_1^{ba}b_{n+1}^\dagger(\underline{k})a_n(\underline{k}) + h.c.] \end{aligned} \quad (14)$$

$$\hat{H}_2^{\text{res}} = \sum_{n,\underline{k}} [-eF(R_0^{ab}a_n^\dagger(\underline{k})b_n(\underline{k}) + R_0^{ba}b_n^\dagger(\underline{k})a_n(\underline{k}))] \quad (15)$$

with the parabolic dispersion $E_k = \hbar^2 k^2 / (2m_w)$ (m_w is the effective mass in the well) and the couplings $R_h^{\nu'\nu} = \int dz \Psi^{\nu'}(z - hd)z\Psi^\nu(z)$. All energies E are given with respect to the bottom of the quantum well. The values of the coefficients are presented in Table 1. The term \hat{H}_2 can be incorporated into the one electron states by diagonalizing $\hat{H}_0 + \hat{H}_2$ [16]. This leads to renormalized field-dependent coefficients in \hat{H}_0 and \hat{H}_1 (which are used in the following) but does not change the structure of the problem for a homogeneous electric field.

\hat{H}^{res} is only considering \underline{k} -conserving processes reflecting an ideal structure with translational invariance in the \underline{r} -plane and neglecting any many-particle processes. Nevertheless, there are non \underline{k} -conserving processes as well which may

$E^a = 47.1 \text{ meV}$	$T_1^a = -0.0201 \text{ meV}$	$R_0^{ba} = -0.149d$
$E^b = 176.6 \text{ meV}$	$T_1^b = 0.0776 \text{ meV}$	$R_1^{ba} = 2.66 \times 10^{-4}d$

Table 1: Calculated level energies and transition elements for Eqs. (13-15).

result from scattering at impurities or interface roughness, e.g.. These give two further contributions to the Hamiltonian:

$$\begin{aligned} \hat{H}_0^{\text{scatter}} = \frac{1}{A} \sum_{\underline{k}, \underline{p}} [& U_0^{aa}(\underline{p}) a_n^\dagger(\underline{k} + \underline{p}) a_n(\underline{k}) + U_0^{bb}(\underline{p}) b_n^\dagger(\underline{k} + \underline{p}) b_n(\underline{k}) \\ & + U_0^{ba}(\underline{p}) b_n^\dagger(\underline{k} + \underline{p}) a_n(\underline{k}) + U_0^{ab}(\underline{p}) a_n^\dagger(\underline{k} + \underline{p}) b_n(\underline{k})] \end{aligned} \quad (16)$$

is the contribution due to scattering within the well and

$$\begin{aligned} \hat{H}_1^{\text{scatter}} = \frac{1}{A} \sum_{\underline{k}, \underline{p}} [& U_1^{aa}(\underline{p}) a_{n+1}^\dagger(\underline{k} + \underline{p}) a_n(\underline{k}) + U_1^{bb}(\underline{p}) b_{n+1}^\dagger(\underline{k} + \underline{p}) b_n(\underline{k}) \\ & + U_1^{ba}(\underline{p}) b_{n+1}^\dagger(\underline{k} + \underline{p}) a_n(\underline{k}) + U_1^{ab}(\underline{p}) a_{n+1}^\dagger(\underline{k} + \underline{p}) b_n(\underline{k}) + h.c.] \end{aligned} \quad (17)$$

refers to interwell scattering, where the restriction to neighboured wells is made.

Within the assumptions of local thermal equilibrium in each well and weak coupling between the wells the current from level ν in well n to level μ in well $n + 1$ is given by the following expression² (see section 9.3 of Ref. [58]):

$$\begin{aligned} I_{n \rightarrow n+1}^{\nu \rightarrow \mu} = 2e \sum_{\underline{k}', \underline{k}} |H_{(n+1)\underline{k}', n\underline{k}}^{\mu, \nu}|^2 \int_{-\infty}^{\infty} \frac{dE}{2\pi\hbar} A_n^\nu(\underline{k}, E) \\ \cdot A_{n+1}^\mu(\underline{k}', E + eFd) [n_F(E - E_n^F) - n_F(E - E_{n+1}^F + eFd)] . \end{aligned} \quad (18)$$

Here E_n^F is the chemical potential in well n which is measured with respect to the bottom of the quantum well. $n_F(x) = (1 + e^{x/(k_B T_e)})^{-1}$ is the Fermi function and T_e is the electron temperature. $A_n^\nu(\underline{k}, E)$ denotes the spectral function for the state \underline{k} of the subband ν in well number n . It represents the weight of the free particle state \underline{k} contributing to the energy E . Then the total density of states $\rho_n^\nu(E)$ in subband ν is given by

$$\rho_n^\nu(E) = \frac{2}{2\pi A} \sum_{\underline{k}} A_n^\nu(\underline{k}, E) \quad (19)$$

where the factor 2 reflects the spin degeneracy and A denotes the sample area. If no scattering is present, the state \underline{k} has a fixed energy $E^\nu + E_k$, and the

²An important point of the derivation is the assumption of uncorrelated scattering in different wells. For example, this is the fact if the electrons are dominantly scattered by the impurities localized in the same well. If the scattering occurs at identical impurities for the electrons in well n and in well $n + 1$ correlation effects occur which may essentially change the result, see Refs. [57, 16].

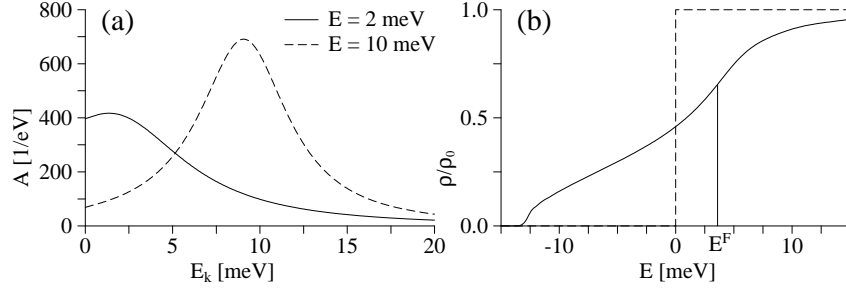


Figure 4: (a) Spectral function $A^a(E_k, E)$ of the lowest level for two different energies E calculated for impurity scattering and interface roughness (see section 6). (b) Density of states in units of the free-particle density of states (dashed line) where we have also indicated the value of the Fermi-energy at zero temperature.

spectral function becomes a δ -function $A_n^\nu(\underline{k}, E) = 2\pi\delta(E - E^\nu - E_k)$. In the continuum limit ($\sum_{\underline{k}} \rightarrow A/(2\pi)^2 \int d^2k$) Eq. (19) gives then the 2-dimensional density of states $\rho_n^\nu(E) = \rho_0\theta(E - E^\nu)$ with $\rho_0 = \frac{m}{\pi\hbar^2}$.

If scattering is present due to $\hat{H}_0^{\text{scatter}}$ the states \underline{k} are no longer eigenstates of the total Hamiltonian. This can be taken into account by calculating the self-energy for the given scattering within standard theory (see, e.g., [58]). Assuming equilibrium the spectral function is then related to the retarded self-energy $\Sigma_n^{\nu \text{ ret}}(\underline{k}, E)$ via

$$A_n^\nu(\underline{k}, E) = \frac{-2\text{Im}\Sigma_n^{\nu \text{ ret}}(\underline{k}, E)}{(E - E^\nu - E_k - \text{Re}\Sigma_n^{\nu \text{ ret}}(\underline{k}, E))^2 + (\text{Im}\Sigma_n^{\nu \text{ ret}}(\underline{k}, E))^2}. \quad (20)$$

Frequently, the self-energy is taken to be constant for simplicity setting $\Sigma_n^{\nu \text{ ret}}(\underline{k}, E) \approx W_n^\nu - i\Gamma_n^\nu/2$. Then the spectral function is a Lorentzian with a full width at half maximum Γ .

Here the self-energies are calculated from basic scattering processes at impurities and interface roughness without using any fitting parameters. This calculation is presented in section 6. The calculated spectral function for different energies E are shown in Fig. 4(a) for illustration. One can clearly see that they exhibit a maximum close to $E_k = E$. From the width we may estimate that $\Gamma \approx 10 \text{ meV}$ holds for $E = 2 \text{ meV}$ and $\Gamma \approx 6 \text{ meV}$ for $E = 10 \text{ meV}$. Fig. 4(b) shows the total density of states.

While the full derivation is slightly tedious [58] formula (18) can be motivated quite easily: In the long-time limit energy has to be conserved during transitions caused by the time-independent interwell couplings $H_{(n+1)\underline{k}', n\underline{k}}^{\mu, \nu}$. Therefore we have to consider tunnelling processes for a certain energy E and integrate over E afterwards. The factor $[n_F(E - E_n^F) - n_F(E + eFd - E_{n+1}^F)]$ takes into account the thermal occupation at the given energy in both wells. The free particle state \underline{k} has a weight $A_n^\nu(\underline{k}, E)/(2\pi)$ in well n . Its transition probability to the state \underline{k}' in well $n + 1$ is given by $2\pi|H_{(n+1)\underline{k}', n\underline{k}}^{\mu, \nu}|^2/\hbar$ (Fermi's golden rule). The final

state has a weight $A_{n+1}^\mu(\underline{k}', E + eFd)/(2\pi)$ at the given energy. Obviously one has to sum over all free particle states $\underline{k}, \underline{k}'$. Finally, the factor 2 is due to the spin degeneracy.

2.1 Resonant Transitions

Let us first investigate the current due to the transition elements from \hat{H}_1^{res} in Eq. (14). They conserve the momentum \underline{k} and therefore the kinetic energy E_k . Using Eq. (19) one can rewrite Eq. (18) as

$$I_{n \rightarrow n+1}^{\nu \rightarrow \mu, \text{res}} = A \frac{e |H_1^{\text{res} \mu, \nu}|^2}{\hbar} \int_{-\infty}^{\infty} dE \rho_n^\nu(E) \langle A_{n+1}^\mu \rangle(E, eFd) [n_F(E - E_n^F) - n_F(E - E_{n+1}^F + eFd)] \quad (21)$$

with the average

$$\langle A_{n+1}^\mu \rangle(E, eFd) = \frac{\sum_{\underline{k}} A_n^\nu(\underline{k}, E) A_{n+1}^\mu(\underline{k}, E + eFd)}{\sum_{\underline{k}} A_n^\nu(\underline{k}, E)}. \quad (22)$$

If the spectral functions are δ -functions $\langle A_{n+1}^\mu \rangle(E, eFd) = 2\pi\delta(E_\nu + eFd - E_\mu)$ holds. Therefore tunnelling only takes place if the levels are exactly aligned. In order to estimate the effect of broadening one may assume constant self-energies $\Sigma_n^{\nu \text{ret}} = -i\Gamma^\nu/2$. Performing the continuum limit and assuming $E - E^\nu \gg \Gamma_n^\nu$ as well as $E + eFd - E^\mu \gg \Gamma^\mu$ one finds

$$\langle A_{n+1}^\mu \rangle(E, eFd) = \frac{\Gamma^\nu + \Gamma^\mu}{(eFd + E^\nu - E^\mu)^2 + (\Gamma^\nu + \Gamma^\mu)^2/4}. \quad (23)$$

This expression has a peak at the resonance $E^\mu = eFd + E^\nu$ and a full width at half maximum of $(\Gamma^\nu + \Gamma^\mu)$. Even if the conditions stated above are not fulfilled, the result is typically similar.

For tunnelling between the lowest levels $a \rightarrow a$, equal densities $E_n^F = E_{n+1}^F$, a constant density of states ρ^a and not too high temperatures and fields $k_B T, eFd < E_n^F - E^a$ one finds

$$I_{n \rightarrow n+1}^{a \rightarrow a} = eA\rho^a \frac{(T_1^a)^2}{\hbar} \frac{2\Gamma^a eFd}{(eFd)^2 + (\Gamma^a)^2}. \quad (24)$$

Therefore the current has a maximum at $eF_{\text{max}}d = \Gamma^a$ where it takes the value $I_{\text{max}} = eA\rho^a(T_1^a)^2/\hbar$. Note that this value neither depends on Γ nor on the Fermi level. Estimating $\Gamma \approx 8$ meV from the spectral functions shown in Fig. 4 and taking $\rho^a = \rho_0$ yields

$$eF_{\text{max}}d \approx 8\text{meV} \quad I_{\text{max}} \approx 0.27\text{mA}. \quad (25)$$

for the $a \rightarrow a$ transition using $T_1^a = -0.0201$ meV from Table 1.

With the translations $2T_1^a \rightarrow E_1$, $E^a \rightarrow E_0$, and $\hbar/\Gamma^a \rightarrow \tau$ Eq. (24) is identical to equation (12)³ of Ref. [10] for the case $E^F > E_0 + E_1$. There

³Note that there is a factor τ missing in the numerator due to a misprint.

semiclassical transport in a miniband for the strong coupling limit $T_1^a \gg \Gamma^a$ was regarded while here the limit of weakly coupled quantum wells $T_1^a \ll \Gamma^a$ is considered. Note that in both derivations the case $(E^F - E^a) > \Gamma^a, 2T_1^a$ is considered.

The transitions from the lowest level to the excited level $a \rightarrow b$ will become important if $eFd \approx E^b - E^a$. Assuming that $k_B T, E_{n+1}^F \ll E^b - E^a$ we find $n_F(E - E_{n+1}^F + eFd) \approx 0$ in this field range. Using the approximation (23) we find close to the resonance

$$I_{n \rightarrow n+1}^{a \rightarrow b} \approx eA n_n^a \frac{|H_1^{\text{res } a, b}|^2}{\hbar} \frac{\Gamma^a + \Gamma^b}{(eFd + E^a - E^b)^2 + (\Gamma^a + \Gamma^b)^2/4}. \quad (26)$$

Note that this current is proportional to the density of carriers $n_n^a = \int dE n_F(E - E_n^F) \rho^a(E)$ in well n while this was not the case for the $a \rightarrow a$ peak in Eq. (24).

2.2 Nonresonant Current

The transition elements from $\hat{H}_1^{\text{scatter}}$ do not conserve momentum and therefore the kinetic energy E_k is changed during the transition. Thus these transitions are not as sensitive to the alignment of the levels as the resonant transition discussed above. They yield a background current which may dominate the current between the resonances. Here only nonresonant transitions via interface roughness are considered. The explicit expressions used are given in section 6. As the actual shape of the interface is not known and may strongly vary for different wafers it has been parameterized by a reasonable set of parameters in order to show the magnitude of the effect. Therefore the reader has to keep in mind that the nonresonant currents can easily vary by a factor of three or even more in the following calculations.

2.3 Calculation of the current

In Eq. (18) the current depends on the electric field and on the Fermi energies in both wells. The Fermi energies E_i^F can easily be calculated from the two-dimensional density of carriers n_i in the well using the relation

$$n_i = \int dE n_F(E - E_i^F) \sum_{\mu} \rho^{\mu}(E). \quad (27)$$

Finally, the total current from well i to well $i+1$ is the sum of the contributions between the different levels.

$$I_{i \rightarrow i+1} = \sum_{\mu, \nu} I_{i \rightarrow i+1}^{\nu \rightarrow \mu} = I(F, n_i, n_{i+1}) \quad (28)$$

The result is presented in Fig. 5 for $n_i = n_{i+1} = N_D$. Neglecting the nonresonant transitions (dashed line) there is a first maximum at $eFd = 9$ meV with a current of 0.277 mA which is in good agreement with the estimation (25) for

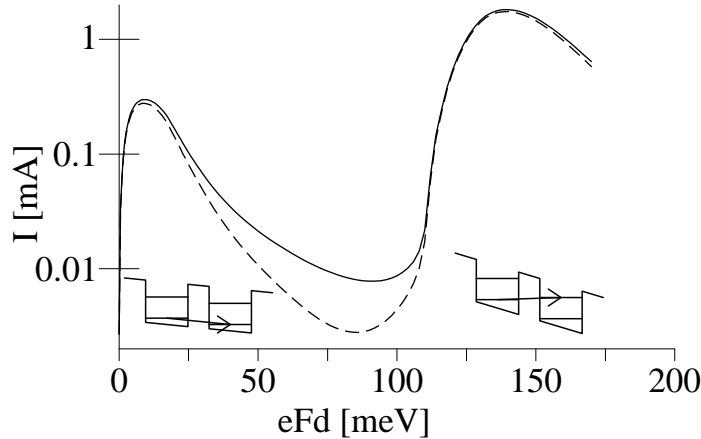


Figure 5: Current $I_{i \rightarrow i+1}$ for $n_i = n_{i+1} = N_D$. The dashed line gives the current from resonant transition, while the full line gives then sum of resonant and nonresonant transitions due to interface roughness.

the $a \rightarrow a$ transitions. A second maximum occurs at $eFd = 140$ meV with $I = 1.75$ mA. In comparison to this the experimental data (see Fig. 6 of [44]) exhibit a first maximum of $I \approx 0.076$ mA and a second maximum of $I \approx 1.45$ mA. While there is good quantitative agreement for the height of second maximum, the calculated first maximum seems to be too large by a factor of 4. This inconsistency will be resolved in the next chapter where the formation of field domains is considered. In contrast to the currents, the position of the maxima is much more difficult to compare as a part of the voltage may drop outside the superlattice. The nonresonant currents are not very large compared to the currents at the maxima but can dominate the total current between the maxima as can be seen from the full line in Fig. 5.

Note that the experimental data of Ref. [44] indicate that the first excited level is unoccupied close to the onset of the $a \rightarrow b$ resonance indicating that the current of approximately 0.1 mA is not carried by the $a \rightarrow b$ transitions there. This may be attributed to stronger nonresonant transition in this field range.

An important feature of the model presented here is the fact that only the nominal sample parameters are involved in the calculation of the currents. The resulting currents are in good quantitative agreement with the experimental data of Refs. [40, 44]. The same model has also been applied to the samples used in Ref. [39] where quantitative agreement could be obtained assuming a smaller barrier width [55]. While these two highly-doped samples exhibit a density of states which resembles the free-electron density of states with a smoothed onset (see Fig. 4), the density of states is much more complicated for low-doped samples due to the presence of impurity bands [59]. Within the single-site approximation for impurity scattering used here (see section 6) these effects are included in the spectral function. The calculation yields a strong dependence of the current on temperature in good agreement with experimental data [60].

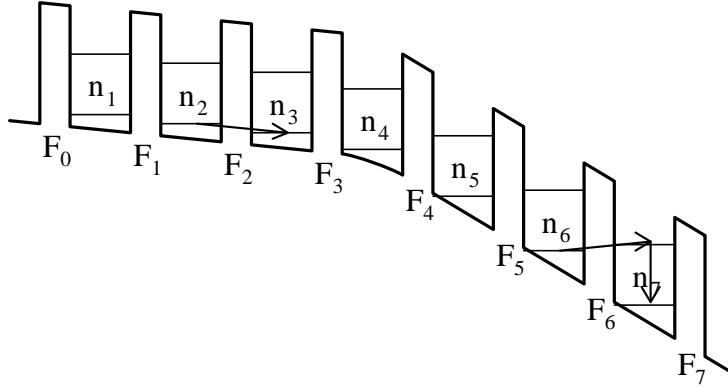


Figure 6: Sketch of the fields and densities for domain formation.

Excellent quantitative agreement has also been found when the sample was irradiated by a strong terahertz field from a free-electron laser source [60]. Therefore we may conclude that the formalism described here allows the quantitative calculation of the currents in weakly-coupled multiple quantum wells for a wide range of samples without applying any fitting parameters.

3 Formation of field domains

Now we want to consider the full structure consisting of N wells numbered $i = 1, \dots, N$ and $N + 1$ barriers. Assuming that the electric field is constant over the structure the total voltage is given by $U \approx (N + 1)Fd$. Fig. 5 shows that $I_{i \rightarrow i+1}(F, N_D, N_D)$ exhibits a region of negative differential conductivity (NDC) between $eF_{\max}d = 9.7$ meV and $eF_{\min}d = 90$ meV. If the electric field is within this NDC-region an instability is likely to occur because a spontaneously formed charge accumulation will increase in time instead of decreasing. This is a common situation for samples exhibiting an N-shaped local current-field relation like the Gunn diode (see, e.g., [19] and references cited therein). In order to include such effects charge accumulation has to be allowed for. This means that the carrier density n_i in well i may deviate from the doping N_D per period. Integrating Poisson's equation over one period yields

$$\epsilon_r \epsilon_0 (F_i - F_{i-1}) = e(n_i - N_D) \quad \text{for } i = 1, \dots, N \quad (29)$$

where F_i is the electric field in the middle of the barrier between wells i and $i + 1$. Here a constant dielectric permeability $\epsilon_r = 13$ is assumed for simplicity.

The notation as well as a typical potential profile is sketched in Fig. 6 for a superlattice with $N = 7$. Within the first wells there is $n_1 = n_2 = n_3 = N_D$ so that $eF_0 = eF_1 = eF_2 = eF_3$. The electric field is low so that the current is dominated by the $a \rightarrow a$ transitions. At well 4 there is charge accumulation $n_4 > N_D$. Therefore we have $eF_4 > eF_3$ and the electric field is large after well 4 so that the current is dominated by the $a \rightarrow b$ resonance. Here we assume

that the electrons relax fast from the upper levels into the lower level which is the only level to be populated in thermal equilibrium for level separations larger than the Fermi energy.⁴

In order to calculate the current between the wells the question arises which electric field should be used if an inhomogeneous situation is considered. As the voltage drop between the wells i and $i + 1$ can be approximated by $eF_i d$ it is natural to use the electric field F_i in the argument of Eq. (28). Nevertheless it has to be stated that this is an approximation done for simplicity and deviations may occur for inhomogeneous field profiles.

Now the temporal evolution of the densities within the wells is given by the continuity equation

$$eA \frac{dn_i}{dt} = I_{(i-1) \rightarrow i} - I_{i \rightarrow (i+1)} = I(F_{i-1}, n_{i-1}, n_i) - I(F_i, n_i, n_{i+1}) \quad (30)$$

for $i = 1, \dots, N$. In order to obtain a complete set of equations for the temporal evolution of the densities and fields we have to add two more features. At first the voltage condition is now given by

$$U = \int dz F(z) \approx \sum_{i=0}^N dF_i + U_c \quad (31)$$

where U_c represents the voltage drop outside the superlattice, which is neglected in the following in order to concentrate on the features of the pure superlattice. At second the currents $I_{0 \rightarrow 1}$ and $I_{N \rightarrow (N+1)}$ across the first and the last barrier of the structure, respectively, have to be specified. For simplicity one may use the expression (28) with appropriate effective densities

$$n_0 = n_0(F_0, N_D, n_1) \quad \text{and} \quad n_{N+1} = n_{N+1}(F_N, N_D, n_N). \quad (32)$$

In mathematical terms the functions $n_0(F_0, N_D, n_1)$ and $n_{N+1}(F_N, N_D, n_N)$ then represent the boundary conditions of the model. Eqs. (29-32) form a complete set of equations for calculating the densities, fields, and currents as a function of time for fixed bias voltage U and given initial conditions $n_i(t_0)$ ($i=1, \dots, N$).

Using a different approach for evaluating the current function $I(F_i, n_i, n_{i+1})$ (which is essentially based on the broadening due to the tunnelling time for the $a \rightarrow b$ resonance and miniband conduction for the $a \rightarrow a$ resonance) and the boundary conditions $n_0(F_0, N_D, n_1) = n_1$, $n_{N+1}(F_N, N_D, n_N) = n_N$ such a model has been used in Ref. [53] to calculate the current-voltage characteristics under domain formation. The model of Ref. [54] uses the boundary condition $n_0(F_0, N_D, n_1) = N_D$ and the current expression

$$I_{i \rightarrow (i+1)} = eA n_i v(F_i) \quad (33)$$

⁴Furthermore the intersubband relaxation must be fast enough to guarantee thermal equilibrium between the levels. If the level separation is larger than the optical phonon energy 36 meV, the intersubband relaxation time is of the order of 1 ps[61], which is typically much faster than the tunnelling times. But for wide quantum wells the level separation becomes small and nonequilibrium effects are found[62].

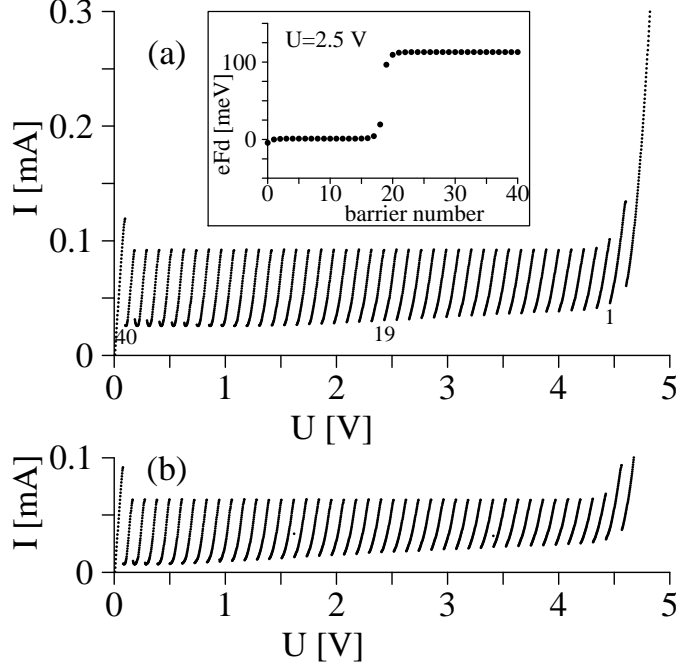


Figure 7: Calculated current-voltage characteristic exhibiting field domains for voltage sweep-up for the boundary conditions $n_0 = 3N_D$ and $n_{N+1} = 3N_D$ with (a) and without (b) nonresonant transitions due to interface roughness. The inset gives the field distribution at $U = 2.5$ V where the domain boundary is located at the 19th well.

where $v(F)$ is a phenomenological tunnelling rate yielding an N-shaped characteristic as shown in Fig. 5. This simplification allows the analytical construction of the full current-voltage characteristic [54, 63]. Eq. (33) is motivated by Eq. (26) for the $a \rightarrow b$ transitions and higher resonances as well. Nevertheless, it seems to be questionable close to the $a \rightarrow a$ maximum as the maximum current of Eq. (24) is independent of n_i for equal carrier densities in adjacent wells. The reason for this deviation is the existence of backward currents for low fields which are taken into account by the factor $[n_F(E - E_n^F) - n_F(E - E_{n+1}^F + eFd)]$ in Eq. (18). If on the other hand $eFd \gg E_{n+1}^F - E^a + k_B T_e$ so that $n_F(E - E_{n+1}^F + eFd) \approx 0$ for all relevant energies E , Eq. (33) is a reasonable approximation.

3.1 Numerical results

In a first simulation the boundary conditions $n_0(F, N_D, n_1) = n_{N+1}(F, N_D, n_N) = 3N_D$ are used. The stationary stable states are determined by simulating Eqs. (29-32) until a stationary state is reached for given U . Increasing or decreasing U afterwards simulates a sweep-up or sweep-down of the voltage, respectively. The result is shown in Fig. 7(a). We find that the characteristic

consists of 40 branches, equal to the number of quantum wells. The maximum current within the branches is about 0.09 mA in good agreement with the experimental situation [40, 42] where around 0.06 mA is observed. This current is significantly lower than the first maximum of $I(F, N_D, N_D)$ (see Fig. 5) resolving the discrepancy discussed at the end of the last section. Note that another superlattice with the same specification [64] exhibits maximum currents of the branches of 0.14 mA. This indicates that the current is quite sensitive to variations in the sample. The calculation exhibits similar effects. If we ignore the nonresonant transitions the maxima of the branches are found at 0.06 mA as shown in Fig. 7(b), although the height of the maxima in the homogeneous characteristics (see Fig. 5) is almost identical. Thus the extension of the branches are very sensitive to the quality of the interfaces (which causes nonresonant transition via interface roughness). Another uncertainty may be the actual barrier thickness as a variation of one monolayer changes the matrix elements \hat{H}_1 by a factor of 1.4 and therefore the current (which is proportional $H_{i,i+1}^2$) by a factor of 2.

The slope of the branches varies between 1.1 mS and 0.55 mS for low and high voltage in Fig. 7 which is significantly larger than the experimental slopes (see [42]) varying between 0.133 mS and 0.064 mS. This lower slope is responsible for the stronger overlap between the branches yielding pronounced multistability [42]. The discrepancy may be resolved by assuming an appropriate contact voltage U_c in Eq. (31) which will depend on I and the fields at the boundaries. Another possibility might be that further nonresonant transitions alter the shape of the homogeneous characteristics of Fig. 5.

The field distribution shown in the inset of Fig. 7(a) is in good agreement with cathodoluminescence measurements [65] stating that the field distribution consists of one low field and one high field domain where the high field domain is located at the anode. These measurements were performed at the same sample but in the range between the $a \rightarrow b$ and the $a \rightarrow c$ resonance.

Using different boundary conditions almost identical domain branches are observed as shown in Fig. 8. The main difference occurs at the first and last branch which may be changed significantly. Comparing Fig. 8(a,b,c) and Fig. 7(a) shows that the first branch is dominated by the boundary condition $n_{N+1}(F_0, N_D, n_1)$ and the last branch by $n_0(F_N, N_D, n_N)$.

3.2 General aspects of domain formation

Now a qualitative explanation of the domain formation shall be given. First regard Fig. 5. For currents I_0 from the interval $[I_{\min}, I_{\max}]$ where $I_{\max} = 0.30$ mA is the maximum current for low fields and $I_{\min} = 7.8 \mu\text{A}$ is the minimum current for medium fields there are 3 intersections $F_I < F_{II} < F_{III}$ of the $I(eFd)$ curve with I_0 . Unlike F_{II} the fields F_I and F_{III} are in the range of positive differential conductivity (PDC). Therefore charge fluctuations are damped out in spatial regions where the electric field takes the values F_I or F_{III} . The field distribution for $U = 2.5$ V in the inset of Fig. 7(a) now shows that the electric field takes the value $F_i \approx F_I$ for $i \leq 17$ and $F_i \approx F_{III}$ for $i \geq 20$. The small

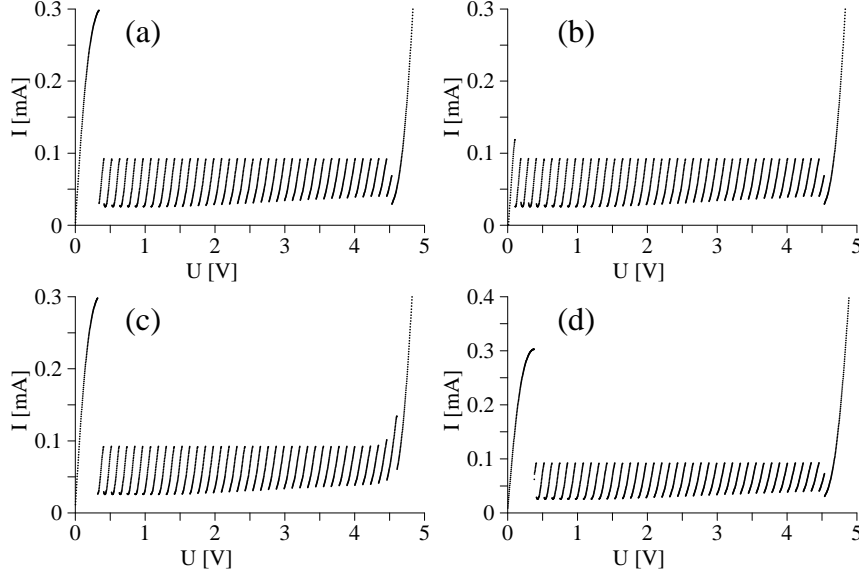


Figure 8: Calculated current-voltage characteristic for voltage sweep-up for the boundary conditions $n_0 = 1.1N_D$, $n_{N+1} = 1.1N_D$ (a), $n_0 = 1.1N_D$, $n_{N+1} = 3N_D$ (b), $n_0 = 3N_D$, $n_{N+1} = 1.1N_D$ (c), and $n_0 = 1.2N_D$, $n_{N+1} = 0.8N_D$ (d)

deviations for $i = 0, 1$ due to the contact are damped out because the field is in the PDC region there. In between there is a domain boundary where the electric field changes due to a charge accumulation $e(n_i - N_D) = \epsilon_r \epsilon_0 (F_i - F_{i-1})$. As the main jump occurs between F_{18} and F_{19} the density n_i takes its maximum at $i_D = 19$. If now this charge accumulation layer is shifted by one period to $i_D = 20$, we have almost the identical situation with the same current except for the fact that the voltage is diminished by $(F_{III} - F_I)d$ as a lower fraction of the sample is in the high field region. This reveals the periodic sequence of branches. If one counts the branches starting from the right side as depicted in Fig. 7(a), the maximum of n_i occurs in well i_D for the i_D th branch. In total one can count 40 branches which is exactly the number of quantum wells as the domain boundary may be located in each well. If the domain boundary comes close to $i = 1$ the low field region is not large enough to shield the variation due to the contact. Therefore the first and the second branch are strongly dependent on the boundary condition which simulates the contact (compare Fig. 7(a) with 8). The field distribution in such stationary domain structures is not arbitrary as the currents across each barrier have to be equal. This provides a condition on the minimal doping density (or minimal carrier generation due to irradiation) as discussed in Refs. [54, 66, 63, 67].

Now the question arises why these stationary domain states are stable while in other spatially extended NDC systems like the Gunn diode typically travelling field domains occur. In Ref. [63] this question has been investigated using the simplified current relation (33). There it could be strictly proven that an

inhomogeneous field distribution is necessarily stable if all electric fields F_i are in the PDC region of $v(F)$ which coincides with most readers' physical intuition. Therefore a field distribution like that in the inset of Fig. 7(a) must be stable if the NDC region $eF_{\max} < eF < eF_{\min}$ is crossed within one jump. Then

$$eF_{i_D-1} \leq eF_{\max} \quad \text{and} \quad eF_{i_D} \geq eF_{\min} \quad (34)$$

holds. In the stationary state the current across each barrier has to be equal to I_0 . Especially, there is $I_0 = I(F_{i_D}, n_{i_D}, n_{i_D+1})$. As F_{i_D} is in the high field region the approximation (33) may be justified yielding $I(F_{i_D}, n_{i_D}, n_{i_D+1}) \approx I(F_{i_D}, N_D, N_D)n_{i_D}/N_D$. Combining this with Poisson's equation $e(n_{i_D} - N_D) = \epsilon_r \epsilon_0 (F_{i_D} - F_{i_D-1})$ exhibits that the condition (34) can be fulfilled if

$$I_0 > I(F_{\min}, N_D, N_D) \left(1 + \frac{\epsilon_r \epsilon_0 (F_{\min} - F_{\max})}{e N_D} \right) \quad (35)$$

holds. It has to be stated that this is only a sufficient condition for stability as there are stable domain states where one field is located within the NDC region. Now I_0 can not be larger than $I(F_{\max}, N_D, N_D)$ as the low field domain can not carry a larger current. Therefore there is a minimum doping density

$$N_{\text{crit}}^{\text{acc}} \sim \frac{\epsilon_r \epsilon_0 (F_{\min} - F_{\max})}{e} \frac{I_{\min}}{I_{\max} - I_{\min}} \quad (36)$$

above which stable domain states with an accumulation layer exist. From the $I(F_i, N_D, N_D)$ relation from Fig. 5 $N_{\text{crit}}^{\text{acc}} \approx 1.2 \times 10^{10}/\text{cm}^2$ is estimated which is much smaller than $N_D = 1.5 \times 10^{11}/\text{cm}^2$. Therefore stable domain states are expected in accordance with the experimental and theoretical findings. Note that the condition (36) depends strongly on I_{\min} which itself is strongly affected by nonresonant transitions as shown in Fig. 5.

Up to now domain structures have been discussed where the high field domain is located at the receiving contact. But of course there is the other possibility that the high field domain is at the injecting contact, i.e., $F_i \approx F_{III}$ for $i < i_D$ and $F_i \approx F_I$ for $i > i_D$. Then Poisson's equation yields a depletion region $n_i < N_D$ at the domain boundary $i \approx i_D$. Such domains have been observed experimentally for highly doped samples [39]. Theoretically, such domains could be both obtained from a simplified model [63] and from the microscopic model [55]. This is shown in Fig. 9 using the parameters of the sample from Ref. [39]. For the boundary conditions $n_0(F_0, N_D, n_1) = 0.95N_D$, $n_{N+1}(F_N, N_D, n_N) = 0.95N_D$ domain states are found, where the high field domain is located at the injecting contact as shown in the inset, while for $n_0(F_0, N_D, n_1) = 1.05N_D$, $n_{N+1}(F_N, N_D, n_N) = 1.05N_D$ the high field domain is located at the receiving contact like in Fig. 7. The domain branches themselves look very similar.

Regarding the stability of such domain structures the argument given above yields a minimum doping

$$N_{\text{crit}}^{\text{dep}} \sim \frac{\epsilon_r \epsilon_0 (F_{\min} - F_{\max})}{e} \frac{I_{\max}}{I_{\max} - I_{\min}} \quad (37)$$

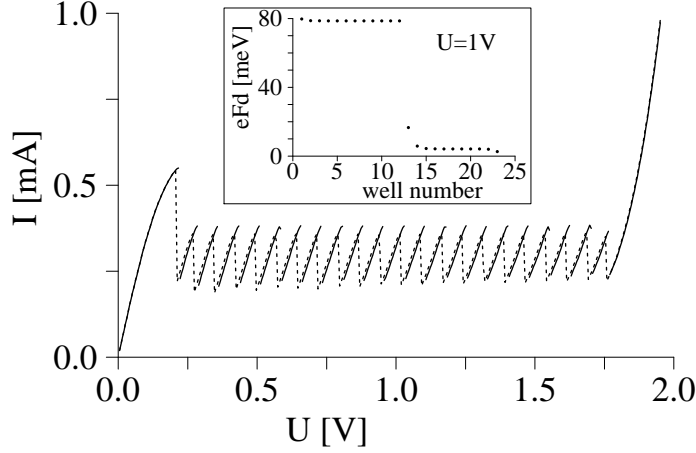


Figure 9: Calculated current-voltage characteristic of the sample from Ref. [39] for voltage sweep-up for the boundary conditions $n_0 = n_{N+1} = 0.95N_D$ (full line), $n_0 = n_{N+1} = 1.05N_D$ (dotted line)

above which stable domain states with a depletion layer can exist. For the sample of Ref. [40] the estimation gives $N_{\text{crit}}^{\text{dep}} \approx 4.4 \times 10^{11}/\text{cm}^2$ which is three times larger than N_D . Thus, such domain states are not expected to be stable and therefore should not be observed. For comparison the sample used in [39] has $N_D = 8.75 \times 10^{11}/\text{cm}^2$ and from Fig. 3 of Ref. [55] $N_{\text{crit}}^{\text{dep}} \approx 2.5 \times 10^{11}/\text{cm}^2$ is estimated in good agreement with the observation of stable domain structures with depletion layers.

Note that the proof of stability essentially relies on the discreteness of the system. In a continuous model the NDC-region can not be crossed without having any fields within this region at least for a small spatial interval. This explains the difference to continuous systems like the Gunn diode where such stable domain states with an arbitrary position of the boundary are not observed.

4 Imperfect Superlattices

All the theoretical current-voltage characteristics shown up to now exhibited an almost regular series of branches whereas in typical experiments the lengths of the branches vary. It is straightforward to assume that this is caused by irregularities in the real superlattice as nothing is perfect. But then the question about the nature of these irregularities arises. At first there are two different possibilities: Regarding a wafer as sketched in Fig. 10 the irregularity may either be a bad spot localized somewhere in the superlattice as shown in the right side of the wafer or a deviation from periodicity occurring in the whole layer. Such deviations may be a larger or smaller barrier width, or a different doping density in certain wells, e.g., which are established due to insufficient control of

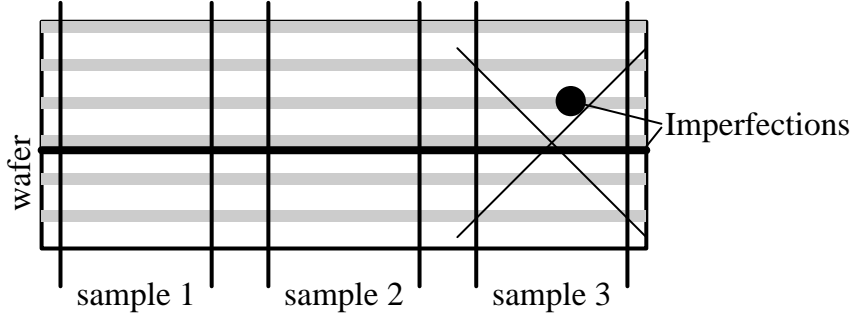


Figure 10: Schematic draw of a superlattice wafer from which 3 different samples are obtained. The dot in sample 3 represents a local imperfection while the line represents a modulation of the periodic structure.

the growth process. Fortunately, one can distinguish these two cases experimentally. If the local spot would be the essential cause for the irregularities in the characteristics, sample 2 and sample 3 from the same wafer sketched in Fig. 10 should exhibit a different modulation of the branches as their individual spots have different sizes and are located at different positions. But the different samples used in [64] exhibited almost identical modulations of the branches if they originated from the same wafers while there are large differences for samples from different wafers even if the superlattice structure is nominally identical. This would be expected from the samples 1 and 2 sketched in Fig. 10. The same feature can be observed in [39] where the authors have fabricated samples with different numbers of periods originating from one wafer by an etching process. They found very similar sequences of longer and shorter branches which allowed them to conclude that the high field domain is located at the receiving contact in their samples.

These experimental observations clearly indicate that the dominant deviations from periodicity are not (x, y) -dependent but extend over the whole wafer. This allows to simulate these irregular superlattices by introducing local fluctuations in the well width, barrier width or doping concentration into Eqs. (18,29). This has been done in Ref. [64] within the model of Ref. [53] where we found that even small spatial fluctuations (about 7%) of the doping have a significant influence on the length of the branches and can explain the observed behaviour. Furthermore, single fluctuations may be located by just determining the number of the branch which is altered most. This effect is particularly pronounced for fluctuations in the barrier width, where a one monolayer fluctuation may change the characteristic significantly. The theoretical prediction has been successfully checked experimentally by growing a new sample exhibiting one barrier with a larger thickness [68].

Now doping fluctuations are included into the model discussed before by using a well-dependent doping density N_{Di} in Eq. (29). The impact on the impurity scattering is neglected, so that the old function $I(F_i, n_i, n_{i+1})$ is used. The result is shown in Fig. 11 and exhibits fluctuating branch heights in ac-

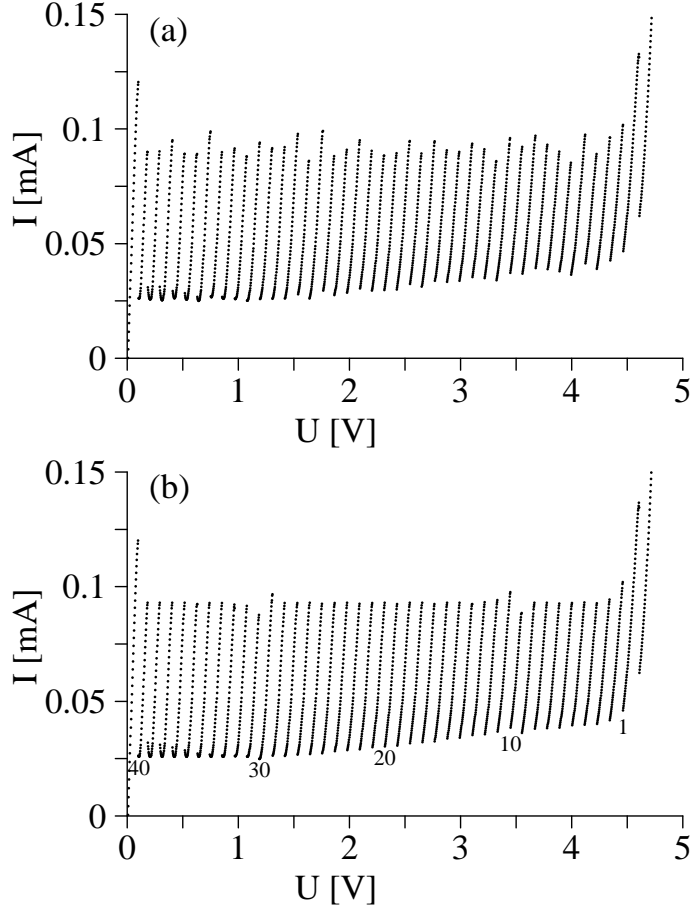


Figure 11: Current-voltage characteristic for doping fluctuations, In (a) a random sequence N_{Di} with an average fluctuation of 10% around N_D is used. In (b) there is $N_{D10} = 1.2N_D$ and $N_{D30} = 0.8N_D$ while the other densities are not altered.

cordance with the model used in Ref. [64]. Comparing the local fluctuations N_{Di} with the maximum current of the branch, one finds a correlation. Like the findings of Ref. [69] the branch $i + 1$ counted from the right extends to higher currents if N_{Di} is larger than N_D . Additionally the branch i extends to lower currents as can be seen from Fig. 11(b). The deviations in the current seem to be smaller and the effects to neighbored branches seem to be larger here than observed in Refs. [64, 69]. This might be related to the fact that a higher doping density was used in previous works.

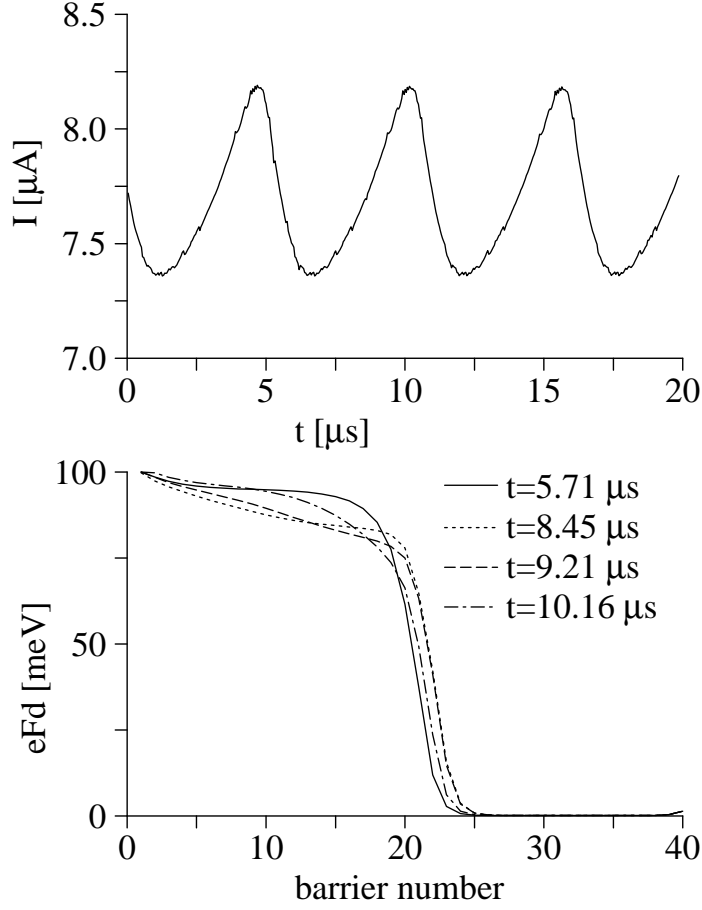


Figure 12: Calculated current oscillations for $U = 2$ V.

5 Oscillatory behaviour

Oscillatory behaviour has been observed in coupled multiple quantum wells both experimentally [26, 27, 28] and theoretically [29, 30]. As an example such behaviour is obtained within the model discussed here for the boundary conditions $n_0(F, N_D, n_1) = 0.8N_D$ and $n_{N+1}(F, N_D, n_N) = 1.2N_D$ which is just the reversed sequence used for the calculation of Fig. 8(d) where stable domain branches were found. Fig. 12 shows self-sustained current oscillations between $7.4 \mu\text{A}$ and $8.2 \mu\text{A}$ with a frequency of 0.18 MHz . Similar results are obtained for different biases and different values $n_0(F, N_D, n_1) < N_D$. The oscillations may be described from the field distribution as follows. At $t = 5.71 \mu\text{s}$ the field distribution consists of a high field and a low field domain with a depletion layer in between. As for $N_D < N_{\text{crit}}^{\text{dep}}$ such a distribution is not stable the boundary travels to the right thereby decreasing the electric field in the high field domain

because the total voltage has to remain constant ($t = 8.45\mu\text{s}$). As the high field domain enters now the region of NDC for $eFd < 90$ meV a new positive charge accumulation layer is created there which is slightly visible for $t = 9.21\mu\text{s}$ at $i \approx 10$. This accumulation layer travels to the right and increases in time ($t = 10.16\mu\text{s}$) until it merges with the old depletion layer. Then the cycle is repeated again. Such an oscillation type has been described in Ref. [31] within the approximation (33). The very same behaviour happens for charge accumulation layers as well if domain states with an accumulation layer are unstable. For a full treatment of this oscillation type see Ref. [32]. Note that the minimum current in this oscillation cycle roughly coincides with $I(F_{\min}, N_D, N_D)$. This relation seems to hold generally as checked by altering the nonresonant current and thereby $I(F_{\min}, N_D, N_D)$. Therefore the temporal minimum of this type of current oscillation provides information about $I(F_{\min}, N_D, N_D)$ which is strongly dependent on the nonresonant transitions.

In order to study the influence of the boundary conditions onto the oscillations we use the ohmic contact currents $I_{0 \rightarrow 1} = \sigma e F_0 d$ and $I_{N \rightarrow N+1} = \sigma e F_N d$ in the following. For $\sigma = 0.5$ mA/eV a completely different oscillation mode is found as shown in Fig. 13. Here one oscillation cycle consists of the nucleation and travelling of a dipole domain which vanishes by leaving the sample at the receiving contact. The scenario is completely analogous to that described in [70] for a continuous system exhibiting NNDC. Additionally, small current spikes appear which are related to the motion of the accumulation layer from one well to the next as discussed in Ref. [71] for the domain formation process. Thus, these spikes reflect the discreteness of the superlattice.

Experimentally, the sample discussed here also exhibits self-sustained current oscillations if a positive bias is applied at the top contact while there are stable domain branches for a negative bias. The experimental data [31] exhibit current oscillations between $20 \mu\text{A}$ and $35 \mu\text{A}$ with a frequency of 0.4 MHz at $U = 0.78$ V. Thus, the theory is in qualitative agreement with the experiment regarding the oscillations as well. As we did not try and model the contact currents microscopically (which strongly influence the type of oscillations) we can not expect quantitative agreement. Additionally, the shape of the oscillations as well as the frequency depends substantially on the full shape of the current-field relation which is strongly affected by the nonresonant transitions between the resonances. Furthermore, deviations from periodicity may affect the oscillations as well [64, 72].

For larger values of σ (say $\sigma \gtrsim 3$ mA/eV) the same domain branches like those shown in Fig. 8 are found. This indicates that the domain branches themselves are almost identical if their formation is allowed for by the contact conditions and if the doping is sufficiently large. On the other hand the oscillatory behaviour does strongly depend on the exact contact conditions.

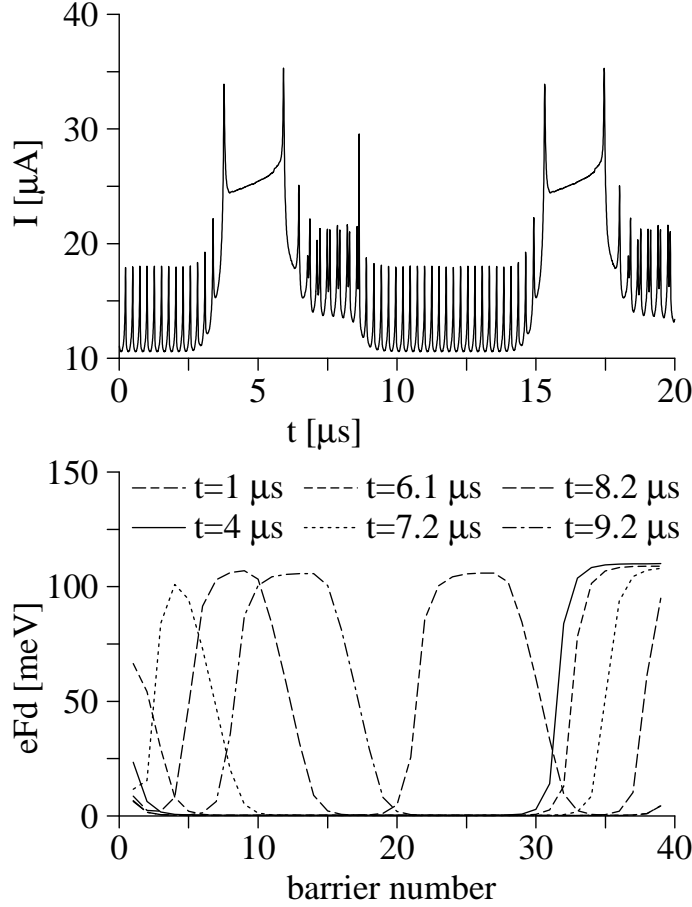


Figure 13: Calculated current oscillations for $U = 1$ V using ohmic boundary conditions with $\sigma = 0.5$ mA/eV.

6 Details of the calculations

In this last section I want to present the details of the calculations whose results have been shown before.

6.1 Calculation of the couplings

In order to calculate the coefficients of Table 1 for Eqs. (13-15) we have to specify the band structure in GaAs and AlAs at first. It is assumed that only the Γ band is of importance. While one may use a parabolic band structure for $\text{Al}_x\text{Ga}_{1-x}\text{As}/\text{GaAs}$ heterostructures for small x this is not appropriate for an GaAs/AlAs heterostructure as the conduction band of GaAs is located far in the band gap of AlAs where the band structure is clearly not parabolic (see Ref. [73]). Following Ref. [74] we model the nonparabolicity by an energy

dependent effective mass $m(E) = m_c(1 + (E - E_c)/E_g)$, where m_c is the effective mass at the conduction band minimum of energy E_c , and E_g is the energy gap. Then the usual connection rules

$$\varphi(z_0 - \varepsilon) = \varphi(z_0 + \varepsilon) \quad (38)$$

$$\frac{1}{m(E, z_0 - \varepsilon)} \frac{d\varphi}{dz}(z_0 - \varepsilon) = \frac{1}{m(E, z_0 + \varepsilon)} \frac{d\varphi}{dz}(z_0 + \varepsilon) \quad (39)$$

hold for the envelope function $\varphi(z)$ provided that the momentum matrix element $P = \hbar\sqrt{E_g/(2m_c)}$ between the conduction and valence band states is identical in both materials. We use the values [74] $m_c^{\text{GaAs}} = 0.067m_e$, $m_c^{\text{AlAs}} = 0.15m_e$, $E_g^{\text{GaAs}} = 1.52$ eV, $E_g^{\text{AlAs}} = 3.13$ eV, and the conduction band discontinuity $\Delta E_c = 1.06$ eV. These parameters yield a relation $E(k) = E_c + \hbar^2 k^2/(2m(E))$ which is in excellent agreement with the band structure of AlAs[73] for the energies of interest. It must be stated that for these parameters the value of P is slightly different for the two materials in contrast to the assumption. Nevertheless, these parameters seem to give reasonable agreement with experimental data both in Ref. [74] and the calculations presented here.

Imposing the Bloch condition $\varphi_q^\nu(z + d) = e^{iqd}\varphi_q^\nu(z)$ the Bloch functions $\varphi_q^\nu(z)$ and eigenvalues E_q^ν are calculated within the Kronig-Penney model. The phase of the Bloch functions is chosen in the following way [6]: Let $z = 0$ be the center of one quantum well. If $\varphi_0^\nu(0) \neq 0$ we chose the phase in such a way that $\varphi_q^\nu(0)$ is real for each q . For $\varphi_0^\nu(0) = 0$, $\varphi_q^\nu(0)$ is chosen to be purely imaginary. Furthermore $\varphi_q^\nu(z)$ has to be an analytic function in q for both cases. From Eq. (2) the level energies E^ν and couplings T_1^ν are obtained. Eq. (1) provides the Wannier functions which are plotted in Fig. 2. Finally, the couplings $R_h^{\nu'\nu}$ are obtained from their definitions $R_h^{\nu'\nu} = \int dz \Psi^{\nu'}(z - hd)z\Psi^\nu(z)$. The calculated values are given in Table 1. A complication arises due to the fact that the effective Hamiltonian of the Kronig-Penney model is energy dependent due to the energy dependence of the effective mass. Therefore the envelope functions $\varphi_q^\nu(z)$ for different energies E_q^ν are not strictly orthogonal but exhibit a small overlap which is neglected in the calculation.

6.2 Impurity scattering

Here we want to calculate the self-energy⁵ for impurity scattering. The contribution to $\hat{H}_0^{\text{scatter}}$ of Eq. (16) for the lowest level a is given by

$$\hat{H}_0^{\text{imp}} = \frac{1}{A} \sum_{\underline{k}, \underline{p}, i, n} V_{i,n}^{aa}(\underline{p}) a_n^\dagger(\underline{k} + \underline{p}) a_n(\underline{k}) \quad (40)$$

Here the subscript i denotes the impurity located at the position (\underline{r}_i, z_i) . The matrix element is calculated with the Wannier functions yielding:

$$V_{i,n}^{aa}(\underline{p}) = \int d^2r dz e^{-i\underline{p} \cdot \underline{r}} \Psi_a^*(z) \Psi_a(z) \frac{-e^2}{4\pi\epsilon_s\epsilon_0 \sqrt{|\underline{r} - \underline{r}_i|^2 + (z - z_i + nd)^2}}$$

⁵For readers who are not familiar with the concepts of many particle physics (such as self-energies, Green functions, etc.) Ref. [75] is recommended as a helpful introduction.

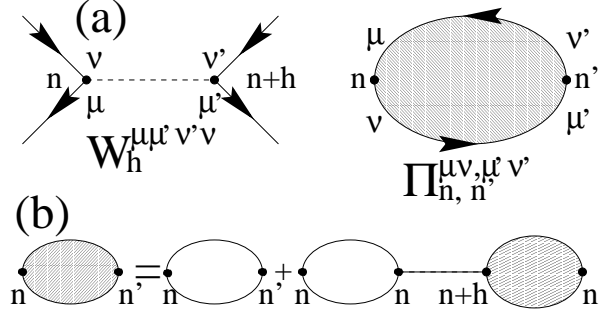


Figure 14: a) gives the notation of the matrix element $W_h^{\mu\mu'\nu'\nu}(\underline{p})$ and the polarizability $\Pi_{n,n'}^{\mu\nu,\mu'\nu'}(\underline{p}, \omega = 0)$. b) shows the random-phase approximation diagrammatically

$$= \frac{-e^2}{2\epsilon_s\epsilon_0 p} \int dz \Psi_a^*(z) \Psi_a(z) e^{-p|z-z_i+nd|} e^{-i\underline{p}\cdot\underline{r}_i}. \quad (41)$$

Note that the contribution for $p = 0$ is canceled by the respective part in the electron-electron interaction as usual if the number of donors is equal to the number of carriers in the whole sample. In order to prevent the divergence of the matrix element for $p \rightarrow 0$ screening due to the electron-electron interaction has to be considered. (This is a general problem for the Coulomb interaction, see also chapters 5 and 6.) The Hamiltonian for the electron-electron interaction reads:

$$\begin{aligned} \hat{H}^{ee} = & \frac{1}{2A} \sum_{\underline{k}, \underline{k}', \underline{p}, n, h} W_h^{aaaa}(\underline{p}) a_n^+(\underline{k} + \underline{p}) a_{n+h}^+(\underline{k}' - \underline{p}) a_{n+h}(\underline{k}') a_n(\underline{k}) \\ & + \text{terms with b.} \end{aligned} \quad (42)$$

Here we assumed that the overlap of wave functions from different wells is negligible, so that pairs always have to be inside the same well. The matrix element reads:

$$\begin{aligned} W_h^{\mu\mu'\nu'\nu}(\underline{p}) = & \frac{e^2}{2\epsilon_s\epsilon_0 p} \int dz_1 \int dz_2 \Psi^{\mu*}(z_1) \Psi^{\mu'*}(z_2 - dh) \\ & \times \Psi^{\nu'}(z_2 - dh) \Psi^{\nu}(z_1) e^{-p|z_1 - z_2|} \end{aligned} \quad (43)$$

The screening is described by the polarizability $\Pi_{n,n'}^{\mu\nu,\mu'\nu'}(\underline{p}, \omega = 0)$, where ν, μ take the values a and b . The notation follows Ref. [76], where a similar problem is investigated, and is shown in Fig. 14. As the \underline{p} dependence is identical in all parts, we omit it in the notation. Within the random-phase approximation (RPA) we have the Dyson equation (see, e.g., Ref. [58]):

$$\Pi_{n,n'}^{\mu\nu,\mu'\nu'} = \Pi_n^{0\mu\nu} \left(\delta_{n,n'} \delta_{\mu,\nu'} \delta_{\nu,\mu'} + \sum_{h,\mu'',\nu''} W_h^{\nu\mu''\nu''\mu} \Pi_{n+h,n'}^{\mu''\nu'',\mu'\nu'} \right) \quad (44)$$

where the vacuum polarizability Π^0 is given by [58]

$$\Pi_n^{0\mu\nu}(\underline{p}, \omega = 0) = \frac{2}{A} \sum_{\underline{k}} \frac{n_F(E_{\underline{k}+\underline{p}} + E^\nu - E_n^F) - n_F(E_{\underline{k}} + E^\mu - E_n^F)}{(E_{\underline{k}+\underline{p}} + E^\nu) - (E_{\underline{k}} + E^\mu)}. \quad (45)$$

Now we find that $\Pi_n^{0bb}(\underline{p}, \omega = 0) = 0$ assuming that the upper level is not occupied. $\Pi_n^{0ab}(\underline{p}, \omega = 0)$ is quite small as the gap appears in the denominator. It remains the contribution $\Pi_n^{0aa}(\underline{p}, \omega = 0)$ which yields for the 2 dimensional electron gas [77]:

$$\Pi_n^{0aa}(\underline{p}, \omega = 0) = -\frac{m}{\pi\hbar^2} \left(1 - \Theta(p - 2k_F) \sqrt{1 - 4\frac{k_F^2}{p^2}} \right) \quad (46)$$

which is independent of p for $p < 2k_F$. As all polarizations only have a -indices we omit these indices in the following. Eq. (44) can be solved by a Fourier transformation (for an infinite superlattice and assuming $\Pi_n^0 = \Pi^0$ is independent of n). Defining $\tilde{\Pi}_q = \sum_{n'} \Pi_{n,n'} e^{iq(n'-n)}$, $\tilde{W}_q^{aaaa} = \sum_h W_h^{aaaa} e^{iqh}$ we find

$$\tilde{\Pi}_q = \frac{\Pi^0}{1 - \Pi^0 \tilde{W}_q^{aaaa}}. \quad (47)$$

Now the screened electron-impurity interaction is given by the bare interaction and a part combined with the polarizability given by

$$V_{i,n}^{aasc}(\underline{p}) = V_{i,n}^{aa} + \sum_{h,n'} W_h^{aaaa} \Pi_{n+h,n'} V_{i,n'}^{aa}. \quad (48)$$

Defining $\tilde{V}_{i,q}^{aa} = \sum_n V_{i,n} e^{-iq(n-n_i)}$ and using the translational invariance $\Pi_{n+h,n'} = \Pi_{2n+h-n',n}$ we find:

$$V_{i,n}^{aasc}(\underline{p}) = \frac{1}{2\pi} \int_{-\pi}^{\pi} dq \frac{\tilde{V}_{i,q}^{aa}}{1 - \Pi^0 \tilde{W}_q^{aaaa}} e^{iq(n-n_i)} \quad (49)$$

Similarly we have:

$$\begin{aligned} V_{i,n}^{bbsc}(\underline{p}) &= V_{i,n}^{bb} + \sum_{h,n'} W_h^{baab} \Pi_{n+h,n'} V_{i,n'}^{aa} \\ &= \frac{1}{2\pi} \int_{-\pi}^{\pi} dq \left[\frac{\tilde{V}_{i,q}^{bb}}{1 - \Pi^0 \tilde{W}_q^{aaaa}} + \frac{(\tilde{W}_q^{baab} \tilde{V}_{i,q}^{aa} - \tilde{W}_q^{aaaa} \tilde{V}_{i,q}^{bb}) \Pi^0}{1 - \Pi^0 \tilde{W}_q^{aaaa}} \right] e^{iq(n-n_i)}. \end{aligned} \quad (50)$$

The screened matrix elements from Eqs. (49,50) are used in the Hamiltonian (40) in the following.

Now we calculate the self energy within the single-site approximation which is shown diagrammatically in Fig. 15. For the impurity i we find the contribution

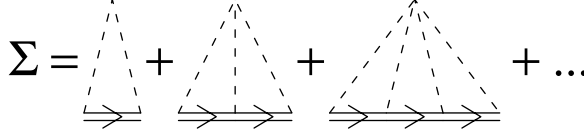


Figure 15: Diagrams contained in the self-consistent single-site approximation

to the self energy $\Sigma_n^{a \text{ ret}}(\underline{k}, E)$

$$\begin{aligned} \Sigma_n^{a,i}(\underline{k}, E) = & \frac{1}{A^2} \sum_{\underline{k}_1} V_{i,n}^{aa \text{ sc}}(\underline{k} - \underline{k}_1) G(\underline{k}_1, E) V_{i,n}^{aa \text{ sc}}(\underline{k}_1 - \underline{k}) \\ & + \frac{1}{A^3} \sum_{\underline{k}_1, \underline{k}_2} V_{i,n}^{aa \text{ sc}}(\underline{k} - \underline{k}_1) G(\underline{k}_1, E) V_{i,n}^{aa \text{ sc}}(\underline{k}_1 - \underline{k}_2) G(\underline{k}_2, E) V_{i,n}^{aa \text{ sc}}(\underline{k}_2 - \underline{k}) \\ & + \frac{1}{A^4} \sum_{\underline{k}_1, \underline{k}_2, \underline{k}_3} V_{i,n}^{aa \text{ sc}}(\underline{k} - \underline{k}_1) G(\underline{k}_1, E) V_{i,n}^{aa \text{ sc}}(\underline{k}_1 - \underline{k}_2) G(\underline{k}_2, E) \\ & \times V_{i,n}^{aa \text{ sc}}(\underline{k}_2 - \underline{k}_3) G(\underline{k}_3, E) V_{i,n}^{aa \text{ sc}}(\underline{k}_3 - \underline{k}) + \dots \end{aligned} \quad (51)$$

where $G(\underline{k}, E) = (E - E_k - \Sigma_n^{a \text{ ret}}(\underline{k}, E))^{-1}$ is the full retarded Green function. This sum can be transformed to the self-consistent equation (see, e.g., [59])

$$K^{a,i}(\underline{k}_1, \underline{k}, E) = V_{i,n}^{aa \text{ sc}}(\underline{k}_1 - \underline{k}) + \frac{1}{A} \sum_{\underline{k}_2} V_{i,n}^{aa \text{ sc}}(\underline{k}_1 - \underline{k}_2) G(\underline{k}_2, E) K^{a,i}(\underline{k}_2, \underline{k}, E) \quad (52)$$

which can be solved numerically for a given self-energy function $\Sigma_n^{a \text{ ret}}(\underline{k}, E)$ entering $G(\underline{k}_2, E)$. The contribution to the self energy is then given by

$$\Sigma_n^{a,i}(\underline{k}, E) = \frac{1}{A^2} \sum_{\underline{k}_1} V_{i,n}^{aa \text{ sc}}(\underline{k}_1 - \underline{k}) G(\underline{k}_1, E) K^{a,i}(\underline{k}_1, \underline{k}, E). \quad (53)$$

Summing up the contribution from all impurities i and possibly different scattering processes we obtain the self-energy function

$$\Sigma_n^{a \text{ ret}}(\underline{k}, E) = \sum_i \Sigma_n^{a,i}(\underline{k}, E) + \Sigma_n^{a, \text{other scattering}}(\underline{k}, E). \quad (54)$$

Now a self consistent solution of Eqs. (52,53,54) can be achieved by iteration.

The contribution to $\Sigma_n^{b \text{ ret}}(\underline{k}, E)$ is calculated in the same way.

6.3 Interface roughness

Interface roughness is modelled like in Ref. [56] considering an interface located at $z = z_0$ exhibiting thickness fluctuations $\xi(\underline{r})$ of the order of $\pm\eta$ (we use $\eta = 2.8 \text{ \AA}$ which is one monolayer of GaAs). We assume the correlations

$$\langle \xi(\underline{r}) \rangle_r = 0 \quad (55)$$

$$\langle \xi(\underline{r}) \xi(\underline{r}') \rangle_r = \alpha \eta^2 \exp(-|\underline{r} - \underline{r}'|/\lambda) \quad (56)$$

with a correlation length $\lambda = 7$ nm and an average coverage $\alpha = 0.5$. Such an exponential correlation function $\langle \xi(\underline{r})\xi(\underline{r}') \rangle_r$ seems to be more appropriate than the usual choice of a Gaussian (see, e.g., Ref. [78]) as stated in Refs. [79, 56]. Like in Ref. [78] (where the scattering of Bloch states in a superlattice is regarded) the additional potential⁶ due to the roughness is modelled by a δ -function at the perfect interface

$$U(\underline{r}, z) = \xi(\underline{r})\Delta E_c \delta(z - z_0). \quad (57)$$

This gives the following interface roughness contribution to \hat{H}^{scatter}

$$\begin{aligned} \hat{H}^{\text{rough}} = \frac{1}{A} \sum_{\underline{k}, \underline{p}, h} & \left[U_h^{aa}(\underline{p}) a_{n+h}^\dagger(\underline{k} + \underline{p}) a_n(\underline{k}) + U_h^{bb}(\underline{p}) b_{n+h}^\dagger(\underline{k} + \underline{p}) b_n(\underline{k}) \right. \\ & \left. + U_h^{ba}(\underline{p}) b_{n+h}^\dagger(\underline{k} + \underline{p}) a_n(\underline{k}) + U_h^{ab}(\underline{p}) a_{n+h}^\dagger(\underline{k} + \underline{p}) b_n(\underline{k}) \right] \end{aligned} \quad (58)$$

with the matrix elements

$$U_h^{\nu\mu}(\underline{p}) = \int d^2 r e^{-i\underline{p}\cdot\underline{r}} \Delta E_c [\xi(\underline{r}) \Psi^{\nu*}(z_0 - hd) \Psi^\mu(z_0)] . \quad (59)$$

Using the correlation function (56) we obtain the square of the matrix element

$$|U_h^{\nu\mu}(\underline{p})|^2 = A \Delta E_c^2 |\Psi_\nu(z_0 - hd)|^2 |\Psi_\mu(z_0)|^2 \frac{2\pi\alpha\eta^2\lambda^2}{(1 + (p\lambda)^2)^{3/2}} \quad (60)$$

which enters the expressions in the following.

The elements $U_0^{\nu\mu}$ result in scattering within the wells. Their contribution to the self-energy is calculated within the self-consistent Born approximation (which is just the first diagram of the infinite sum in Fig. 15)

$$\Sigma_{\text{rough}}^{a \text{ ret}}(\underline{k}, E) = \frac{2}{A^2} \sum_{\underline{k}_1} |U_0^{aa}(\underline{k} - \underline{k}_1)|^2 G(\underline{k}_1, E), \quad (61)$$

where the factor 2 takes into account the two interfaces per well. These self-energies contribute to the total self energy in Eq. (54). The calculation for the subband b is performed in the same way.

The elements $U_1^{\nu\mu}$ contribute to the non-resonant current from one well to the next via Eq. (18). Here the contributions from all 4 interfaces of both wells involved are summed up. For weakly coupled wells $U_2^{\nu\mu}, U_3^{\nu\mu}, \dots$ are small and can be neglected.

⁶In chapter 11 of this book the potential is chosen to be the variation of the energy levels due to the well width fluctuation which is only defined for scattering within a given level and a given well. The approach via Eq. (57) has the advantage that interwell and interlevel transitions can be handled as well. For intrawell and intralevel processes the results are similar as $dE^\nu/dw \sim \Delta E_c |\Psi^\nu(z_0)|^2$ where w is the well width and z_0 is the position of the interface.

6.4 Optical phonons

In polar materials like GaAs the polar interaction with optical phonons provides an important scattering process. As the energy $\hbar\omega_0 = 36$ meV is transferred, this process couples electronic states with different energy in contrast to the two scattering mechanism discussed before. This makes the full calculation of the self-energies much more complicated. But fortunately only a restricted number of processes are allowed at low temperatures where only the emission of phonons takes place. Therefore to any electronic state \underline{k} in level ν with energy $E_k + E^\nu$ affected there must be another state at an energy $E_k + E^\nu - \hbar\omega_0$. For the lowest level $\nu = a$ this means that the condition $E_k > \hbar\omega_0$ must be satisfied in order for phonon scattering to be possible. But for small Fermi levels (5.37 meV for the sample considered) these states are far away from any resonant transition so that the neglect of the phonon contribution to the self-energy hardly affects the currents. The situation is different for the second level. Here the states with $E_k \approx 0$ are in resonance with the occupied states in the ground level if the electric field takes the value $eFd \approx E^b - E^a$. Therefore the actual broadening of these states is crucial for the $a \rightarrow b$ resonance. This process is taken into account by calculating the scattering time τ_{ph} for this process following Ref. [61] yielding $\tau_{\text{ph}} = 0.854$ psec for the structure considered here. For the self-energy contribution the constant value

$$\Sigma_{\text{phonon}}^{b\text{ret}}(\underline{k}, E) = -i \frac{\hbar}{2\tau_{\text{ph}}} \quad (62)$$

is used which contributes to the total self energy in Eq. (54) for the level b .

7 Conclusions

In this chapter the electronic transport in weakly coupled multiple quantum wells has been considered. Within the model of sequential tunnelling the currents have been calculated without any fitting parameters taking into account the scattering at impurities and interface roughness. The currents are in good quantitative agreement with experimental data stating the physical relevance of the model.

In the NDC region a homogeneous field distribution is unstable. For the actual doping of the sample considered both stable field-domains and self-sustained current oscillations are found theoretically in good agreement with the experimental observation. The sequence of domain branches is almost independent of the contacts as the influence of the boundaries is shielded by the domain regions where the electric field is in the regime of positive differential conductivity. Therefore the branches contain information about the transport in multiple quantum wells itself which is not spoiled by contacts which are often only poorly defined. Furthermore the domain branches react quite sensitively to local deviations from periodicity which allows for a check of the actual sample quality.

I want to thank Luis Bonilla, Holger Grahm, Ben Hu, Anatoli Ignatov, Antti-Pekka Jauho, Kristinn Johnsen, Jörg Kastrup, Miguel Moscoso, Michael Patra, Frank Prengel, Eckehard Schöll, Georg Schwarz, and Stefan Zeuner for fruitful collaboration and helpful discussions. Financial support from the Deutsche Forschungsgemeinschaft is gratefully acknowledged.

References

- [1] *Semiconductor Superlattices, Growth and Electronic Properties*, edited by H. T. Grahn (World Scientific, Singapore, 1995).
- [2] L. Esaki and R. Tsu, IBM J. Res. Develop. **14**, 61 (1970).
- [3] F. Capasso, K. Mohammed, and A. Y. Cho, Appl. Phys. Lett. **48**, 478 (1986).
- [4] S. Q. Murphy, J. P. Eisenstein, L. N. Pfeiffer, and K. W. West, Phys. Rev. B **52**, 14825 (1995).
- [5] G. Bastard, *Wave Mechanics Applied to Semiconductor Heterostructures* (Les Editions de Physique, Les Ulis Cedex, France, 1988).
- [6] W. Kohn, Phys. Rev. **115**, 809 (1959).
- [7] D. Emin and C. F. Hart, Phys. Rev. B **36**, 7353 (1987).
- [8] R. Tsu and G. Döhler, Phys. Rev. B **12**, 680 (1975).
- [9] S. Rott, N. Lindner, and G. H. Döhler, Superlattices and Microstructures, in print.
- [10] P. A. Lebowitz and R. Tsu, J. Appl. Phys. **41**, 2664 (1970).
- [11] A. A. Ignatov, E. P. Dodin, and V. I. Shashkin, Mod. Phys. Lett. B **5**, 1087 (1991).
- [12] X. L. Lei, N. J. M. Horing, and H. L. Cui, Phys. Rev. Lett. **66**, 3277 (1991).
- [13] A. Sibille, J. F. Palmier, H. Wang, and F. Mollot, Phys. Rev. Lett. **64**, 52 (1990).
- [14] E. Schomburg, A. A. Ignatov, S. Winnerl, J. Grenzer, K. F. Renk, D. G. Pavel'ev, Y. Koschurinov, B. Y. Melzer, V. Ustinov, S. Ivanov, S. S. ov, A. Zhukov, and P. S. Kop'ev, in *Proc. 23rd Int. Conf. Phys. Semicond., Berlin 1996*, edited by M. Scheffler and R. Zimmermann (World Scientific, Singapore, 1996), Vol. 3, pp. 1679–1682.
- [15] H. T. Grahn, K. von Klitzing, K. Ploog, and G. H. Döhler, Phys. Rev. B **43**, 12094 (1991).
- [16] R. F. Kazarinov and R. A. Suris, Sov. Phys. Semicond. **6**, 120 (1972).
- [17] D. Miller and B. Laikhtman, Phys. Rev. B **50**, 18426 (1994).
- [18] B. Laikhtman and D. Miller, Phys. Rev. B **48**, 5395 (1993).
- [19] M. P. Shaw, V. V. Mitin, E. Schöll, and H. L. Grubin, *The Physics of Instabilities in Solid State Electron Devices* (Plenum Press, New York, 1992).

- [20] M. Büttiker and H. Thomas, Phys. Rev. Lett. **38**, 78 (1977).
- [21] M. Büttiker and H. Thomas, Z. Phys. B **34**, 301 (1979).
- [22] A. A. Ignatov, V. I. Piskarev, and V. I. Shashkin, Sov. Phys. Semicond. **19**, 1345 (1985).
- [23] H. LePerson, C. Minot, L. Boni, J. F. Palmier, and F. Mollot, Appl. Phys. Lett. **60**, 2397 (1992).
- [24] K. Hofbeck, J. Grenzer, E. Schomburg, A. A. Ignatov, K. F. Renk, D. G. Pavel'ev, Y. Koschurinov, B. Melzer, S. Ivanov, S. Schaposchnikov, and P. S. Kop'ev, Phys. Lett. A **218**, 349 (1996).
- [25] C. Waschke, H. G. Roskos, K. Schwedler, K. Leo, H. Kurz, and K. Köhler, Phys. Rev. Lett. **70**, 3319 (1993).
- [26] J. Kastrup, R. Klann, H. T. Grahn, K. Ploog, L. L. Bonilla, J. Galán, M. Kindelan, M. Moscoso, and R. Merlin, Phys. Rev. B **52**, 13761 (1995).
- [27] H. T. Grahn, J. Kastrup, R. Klann, K. H. Ploog, and H. Asai, in *Proc. 23rd Int. Conf. Phys. Semicond., Berlin 1996*, edited by M. Scheffler and R. Zimmermann (World Scientific, Singapore, 1996), Vol. 3, pp. 1671–1674.
- [28] N. Ohtani, M. Hosoda, H. Mimura, K. Tominaga, T. Watanabe, K. Fujiwara, and H. T. Grahn, in *Proc. 23rd Int. Conf. Phys. Semicond., Berlin 1996*, edited by M. Scheffler and R. Zimmermann (World Scientific, Singapore, 1996), Vol. 3, pp. 1675–1678.
- [29] L. L. Bonilla, in *Nonlinear Dynamics and Pattern Formation in Semiconductors*, edited by F. J. Niedernostheide (Springer, Berlin, 1995), Chap. 1, pp. 1–20.
- [30] A. Wacker, F. Prengel, and E. Schöll, in *Proc. 22nd Int. Conf. Phys. Semicond., Vancouver 1994*, edited by D. J. Lockwood (World Scientific, Singapore, 1995), Vol. 2, p. 1075.
- [31] J. Kastrup, R. Hey, K. H. Ploog, H. T. Grahn, L. L. Bonilla, M. Kindelan, M. Moscoso, A. Wacker, and J. Galán, Phys. Rev. B **55**, 2476 (1997).
- [32] L. L. Bonilla, M. Kindelan, M. Moscoso, and S. Venakides, SIAM J. Appl. Math. **57** (1997), in print.
- [33] O. M. Bulashenko and L. L. Bonilla, Phys. Rev. B **52**, 7849 (1995).
- [34] Y. Zhang, J. Kastrup, R. Klann, K. H. Ploog, and H. T. Grahn, Phys. Rev. Lett. **77**, 3001 (1996).
- [35] L. Esaki and L. L. Chang, Phys. Rev. Lett. **33**, 495 (1974).
- [36] Y. Kawamura, K. Wakita, H. Asahi, and K. Kurumada, Jpn. J. Appl. Phys. **25**, L928 (1986).

- [37] K. K. Choi, B. F. Levine, R. J. Malik, J. Walker, and C. G. Bethea, Phys. Rev. B **35**, 4172 (1987).
- [38] M. Helm, P. England, E. Colas, F. DeRosa, and S. J. Allen, Jr., Phys. Rev. Lett. **63**, 74 (1989).
- [39] P. Helgesen and T. G. Finstad, in *Proceedings of the 14th Nordic Semiconductor Meeting*, edited by O. Hansen (University of Århus, ADDRESS, 1990), p. 323.
- [40] H. T. Grahn, R. J. Haug, W. Müller, and K. Ploog, Phys. Rev. Lett. **67**, 1618 (1991).
- [41] S. Murugkar, S. H. Kwok, G. Ambrazevicius, H. T. Grahn, K. Ploog, and R. Merlin, Phys. Rev. B **49**, 16849 (1994).
- [42] J. Kastrup, H. T. Grahn, K. Ploog, F. Prengel, A. Wacker, and E. Schöll, Appl. Phys. Lett. **65**, 1808 (1994).
- [43] Y. Zhang, X. Yang, W. Liu, P. Zhang, and D. Jiang, Appl. Phys. Lett. **65**, 1148 (1994).
- [44] S. H. Kwok, H. T. Grahn, M. Ramsteiner, K. Ploog, F. Prengel, A. Wacker, E. Schöll, S. Murugkar, and R. Merlin, Phys. Rev. B **51**, 9943 (1995).
- [45] S. A. Stoklitskii, V. N. Murzin, G. K. Rasulova, Y. A. Mityagin, A. P. Perestoronin, B. Monemar, P. O. Holz, and M. Singh, JETP Lett. **61**, 405 (1995).
- [46] Z. Y. Han, S. F. Yoon, K. Radhakrishnan, and D. H. Zhang, Superlattices and Microstructures **18**, 83 (1995).
- [47] B. J. Keay, S. J. Allen, J. Galán, J. P. Kaminski, K. L. Champman, A. C. Gossard, U. Bhattacharya, and M. J. M. Rodwell, Phys. Rev. Lett. **75**, 4098 (1995).
- [48] S. Zeuner, B. J. Keay, S. J. Allen, K. D. Maranowski, A. C. Gossard, U. Bhattacharya, and M. J. W. Rodwell, Phys. Rev. B **53**, 1717 (1996).
- [49] H. Mimura, M. Hosoda, N. Ohtani, K. Tominaga, K. Fujita, T. Watanabe, H. T. Grahn, and K. Fujiwara, Phys. Rev. B **54**, 2323 (1996).
- [50] R. A. Suris, Sov. Phys. Semicond. **7**, 1030 (1974).
- [51] B. Laikhtman, Phys. Rev. B **44**, 11260 (1991).
- [52] A. N. Korotkov, D. V. Averin, and K. K. Likharev, Appl. Phys. Lett. **62**, 3282 (1993).
- [53] F. Prengel, A. Wacker, and E. Schöll, Phys. Rev. B **50**, 1705 (1994), *ibid* **52**, 11518 (1995).

- [54] L. L. Bonilla, J. Galán, J. A. Cuesta, F. C. Martínez, and J. M. Molera, Phys. Rev. B **50**, 8644 (1994).
- [55] A. Wacker and A.-P. Jauho, Physica Scripta, in print (cond-mat/9610120).
- [56] A. Wacker and A.-P. Jauho, Superlattices and Microstructures, in print (cond-mat/9610119).
- [57] L. Zheng and A. H. MacDonald, Phys. Rev. B **47**, 10619 (1993).
- [58] G. D. Mahan, *Many-Particle Physics* (Plenum, New York, 1990).
- [59] A. Gold, J. Serre, and A. Ghazali, Phys. Rev. B **37**, 4589 (1988).
- [60] A. Wacker, A. Jauho, S. Zeuner, and S. J. Allen, submitted to Phys. Rev. Lett. (cond-mat/9612035).
- [61] R. Ferreira and G. Bastard, Phys. Rev. B **40**, 1074 (1989).
- [62] Y. A. Mityagin, V. N. Murzin, Y. A. Efimov, and G. K. Rasulova, Superlattices and Microstructures, in print.
- [63] A. Wacker, M. Moscoso, M. Kindelan, and L. L. Bonilla, Phys. Rev. B **55**, 2466 (1997).
- [64] A. Wacker, G. Schwarz, F. Prengel, E. Schöll, J. Kastrup, and H. T. Grahn, Phys. Rev. B **52**, 13788 (1995).
- [65] S. H. Kwok, U. Jahn, J. Menniger, H. T. Grahn, and K. Ploog, Appl. Phys. Lett. **66**, 2113 (1995).
- [66] G. Schwarz and E. Schöll, phys. status solidi (b) **194**, 351 (1996).
- [67] Y. A. Mityagin and V. N. Murzin, JEPT Lett. **64**, 155 (1996).
- [68] G. Schwarz, F. Prengel, E. Schöll, J. Kastrup, H. T. Grahn, and R. Hey, Appl. Phys. Lett. **69**, 626 (1996).
- [69] M. Patra, Master's thesis, Technische Universität Berlin, 1996.
- [70] L. L. Bonilla, P. J. Hernando, M. A. Herrero, M. Kindelan, and J. J. L. Velázquez, Asymptotics of the trap-dominated Gunn effect in p-type Ge, submitted to Physica D.
- [71] J. Kastrup, F. Prengel, H. T. Grahn, K. Ploog, and E. Schöll, Phys. Rev. B **53**, 1502 (1996).
- [72] E. Schöll, G. Schwarz, M. Patra, F. Prengel, and A. Wacker, in *Proc. 9th Int. Conf. on Hot Carriers in Semiconductors, Chicago 1995*, edited by K. Hess, J. P. Leburton, and U. Ravaioli (Plenum Press, New York, 1996), pp. 177–181.

- [73] J. N. Schulman and Y.-C. Chang, Phys. Rev. B **31**, 2056 (1985).
- [74] G. Brozak, E. A. de Andrada e Silva, L. J. Sham, F. DeRosa, P. Miceli, S. A. Schwarz, J. P. Harbison, L. T. Florez, and S. J. Allen, Phys. Rev. Lett. **64**, 471 (1990).
- [75] R. D. Mattuck, *A Guide to Feynman Diagrams in the Many Body Problem* (Republication by Dover, New York, 1992).
- [76] G. L. Eliasson, Ph.D. thesis, Brown University, 1987.
- [77] F. Stern, Phys. Rev. Lett. **18**, 546 (1967).
- [78] I. Dharssi and P. N. Butcher, J. Phys.: Condens. Matter **2**, 4629 (1990).
- [79] S. M. Goodnick, D. K. Ferry, C. W. Wilmsen, Z. Liliental, D. Fathy, and O. L. Krivanek, Phys. Rev. B **32**, 8171 (1985).